

The Impact of Lateral Boundary Conditions and Horizontal Resolution on North Atlantic Water Mass Transformations and Pathways in an Isopycnic Coordinate Ocean Model

LINDA T. SMITH, ERIC P. CHASSIGNET, AND RAINER BLECK

Rosenstiel School of Marine and Atmospheric Science, University of Miami, Miami, Florida

(Manuscript received 24 August 1998, in final form 11 March 1999)

ABSTRACT

A series of numerical experiments for the North Atlantic have been carried out with a primitive equation density-coordinate model, incorporating a relaxation zone south of 65°N designed to simulate the production of dense water in regions outside the model domain. The principal experiments vary both the horizontal grid resolution of the model (0.9° and ½°) and the width of the buffer zone (4° and ½°); an additional model experiment addresses the issue of the forcing used within the restoring region. The North Atlantic water mass transformations simulated in the various experiments and the subsequent pathways of converted water from the northern boundary region into the interior basin are documented both by time-evolution and time-mean analysis of the model results, focusing on the mass content of the isopycnic layers, the spread of water masses tagged with a passive tracer, the meridional overturning streamfunction and associated transport of heat, and mass transport budgets within specified density classes. Primarily because of its inherent ability to retain the characteristics of dense water masses, the density-coordinate model is found to be relatively insensitive to the configuration of the northern boundary region when compared to similarly configured models in depth coordinates. However, the density-coordinate experiments with finer grid resolution produce higher values of northward heat transport, particularly north of 35°N, and the strongest meridional overturning and heat transport are seen in an experiment combining wide buffer zones and high horizontal resolution. Comparison to observations indicates that the use of σ_2 rather than σ_θ as the coordinate representation of density, together with refinements in vertical resolution, will likely improve the model's ability to accurately represent the water mass distributions and three-dimensional circulation of the Atlantic.

1. Introduction

The importance attached to studies of the earth's climate ensures that the Atlantic will remain the most scrutinized of the world's oceans, primarily due to its singular properties regarding the transport and redistribution of heat. Warmed by the sun in the Tropics and driven by the winds of each hemisphere, the waters of the Atlantic migrate toward regions of cooling and conversion to dense water masses. The sinking, spreading, and eventual upwelling of these waters of high-latitude origin drive an overturning circulation that spans both hemispheres in the vertical–meridional plane. The associated meridional transport of heat is unique among the world's oceans in maintaining its northward direction from South Atlantic midlatitudes, across the equator, up to the northern subpolar gyre (Bryan 1982; Trenberth and Solomon 1994).

While the densest Atlantic water, Antarctic Bottom

Water (AABW), originates in the high latitudes of the south, it is the North Atlantic Deep Water (NADW) that dominates in the overturning scenario, carrying an estimated 20 Sv (1 Sv $\equiv 10^6 \text{ m}^3 \text{ s}^{-1}$) southward across low northern latitudes within the deep western boundary current (DWBC), versus ~ 4 Sv of AABW crossing the equator into the Northern Hemisphere (McCartney 1993). The NADW has its origins in the subpolar gyre of the North Atlantic and in the Nordic seas, basins of complex geometry and bathymetry. In order to properly capture the details of the meridional overturning and heat transport, a numerical simulation of the three-dimensional Atlantic circulation must properly represent the outflow from these far northern seas, the associated water mass transformations, and the pathways taken into the interior ocean.

Given these objectives, a crucial choice in the process of designing a basin-scale Atlantic numerical simulation is the configuration of the northern boundary region. Inclusion of the North Atlantic high-latitude basins in the model domain requires the explicit simulation of the complex water mass transformations in the Greenland–Iceland–Norwegian (GIN) seas, of the overflow across

Corresponding author address: Ms. Linda T. Smith, RSMAS, University of Miami, 4600 Rickenbacker Cswy., Miami, FL 33149-1098.
E-mail: lsmith@rsmas.miami.edu

the intricate Greenland–Iceland–Scotland (GIS) ridge topography, and of the formation and transport of sea ice. The increased numerical complexity resulting from such a choice is evident in the Atlantic experiments of Roberts et al. (1996), in which the domain extends to 82°N, requiring a 90° rotation of the Mercator grid to deal with the convergence of meridians near the pole, as well as the incorporation of a simple sea ice model. The North Atlantic simulation by Mauritzen and Häkkinen (1999), configured to encompass the Arctic Ocean and ice field, uses a sigma-coordinate ocean model on a curvilinear horizontal grid coupled to an ice model that is both dynamic and thermodynamic.

An alternative model design, adopted in the experiments of the Community Modeling Effort (CME), involves placing a closed northern boundary across the ridge, at ~65°N, and outfitting a specified region equatorward of the boundary with a buffer zone in which temperature and salinity are relaxed to their monthly climatological values (Bryan and Holland 1989; Böning et al. 1996, hereafter BBHD; Chassignet et al. 1996, hereafter CSBB). The relaxation represents processes taking place outside the model domain, such as the production of dense water in the GIN seas, as well as the subsequent entrainment of upper-layer waters that occurs below the GIS ridge. At the southern boundary, placed at ~15°S in order to capture the Atlantic equatorial region, a similar relaxation is intended to simulate the temperature and salinity characteristics of the stacked water masses at that latitude—the northward-flowing Antarctic Intermediate Water overlying the southward flow of NADW, which in turn lies above the AABW that reaches into the North Atlantic.

Experiments with the depth-coordinate GFDL (Geophysical Fluid Dynamics Laboratory) model (Bryan 1969; Cox 1984) as configured for the CME, and with later GFDL/CME versions of varied horizontal resolution and mixing parameterization, have indicated that the model results are highly sensitive to the formulation of the northern boundary region (BBHD). Döscher et al. (1994) showed that relaxation within the buffer zone to the smoothed Levitus (1982) climatology, which fails to represent the sharp temperature gradient that exists in reality in the Denmark Strait, led to weak overturning and heat transport values in comparison to observations in their depth-coordinate experiments. Döscher et al. found that the use of actual Denmark Strait hydrographic data in the northern restoring zones of non-eddy-resolving and marginally eddy-resolving GFDL/CME experiments increased both the overturning strength and the associated northward transport of heat. In sensitivity studies with a regional version of the $\frac{1}{3}^\circ$ GFDL/CME model, Redler and Böning (1997) found that while the use of fully open boundary conditions could affect the upper-layer structure of the subpolar gyre circulation, such conditions had a negligible effect on the strength of the NADW overturning cell when compared to the significant strengthening achieved by the use of hydro-

graphic data within the northern buffer zone, as in the experiments of Döscher et al. Klinck (1995) examined a 5-yr record from the GFDL/CME eddy-resolving model results and found deficiencies in the representation of certain water masses. These deficiencies primarily result from the fact that while the temperature and salinity fields are restored to the initial climatology within the buffer zones, so that the vertical shear of the currents can be recovered through geostrophic adjustment, the barotropic mass fluxes remain free to evolve with the solution away from the solid wall boundaries.

In addition to the restoring condition, the placement of the northern Atlantic boundary region, its latitudinal extent, and the horizontal resolution of the model grid affect the ability of the buffer zone to represent the processes of sinking and spreading of dense water. In examining results of GFDL/CME experiments at 1° , $\frac{1}{3}^\circ$, and $\frac{1}{6}^\circ$ horizontal resolution, in which buffer zone width was uniformly four grid points regardless of grid size, BBHD found that smaller net meridional overturning rates correlated with the narrower northern boundary zones of higher-resolution cases. The GFDL/CME study of Beckmann et al. (1994) found that meridional overturning rates decreased when horizontal resolution increased from $\frac{1}{3}^\circ$ to $\frac{1}{6}^\circ$, even though buffer zones of equal width ($\frac{4}{3}^\circ$) were used in the experiments. Though unable to fully explain this result, Beckmann et al. point out that factors related to the change in grid resolution, such as the magnitude of friction and the associated damping timescale, imply that the northern restoring zones in the two experiments cannot be considered identical even though their latitudinal span is the same.

Both the placement of the restoring zone and the data used therein were considered in configuring the DYNAMO Group (1997) intercomparison exercise for models formulated in depth, density, and sigma vertical coordinates. In the DYNAMO (Dynamics of North Atlantic Models) experiments, the northern model boundary is located at 70°N, poleward of the North Atlantic ridge system, in order to capture the water mass characteristics of that region and explicitly simulate the overflows. Retention of the observed frontal structures within the northern buffer zone, which encompasses the Denmark Strait and portions of the GIN seas lying below the model boundary, is accomplished by restoring temperature and salinity to values obtained by objective analysis of hydrography (primarily from the National Oceanographic Data Center), using the smoothed Levitus (1982) climatology as background (J. Willebrand 1998, personal communication).

The design of the numerical model itself is also an important factor influencing the effectiveness of the zones of relaxation. The outflow of dense water from the Nordic seas and its advection around the North Atlantic subpolar gyre can best be simulated if the model has the ability to preserve the integrity of its densest water masses. In a series of comparisons between me-

dium-resolution Atlantic models in depth and density coordinates, outfitted with restoring zones $\sim 4^\circ$ wide at the northern and southern boundaries as in the original (1°) GFDL/CME experiments, CSBB illustrate the divergence between the deep-water structures of the models' results over time. Both the depth-coordinate GFDL/CME model (Bryan and Holland 1989) and the density-coordinate MICOM (Miami Isopycnic Coordinate Ocean Model: Bleck and Chassignet 1994) should theoretically produce a certain amount of dense water within the model domain as a result of relaxation toward observed temperatures and salinities in the buffer zones. CSBB found that the depth-coordinate model was unable to retain its densest water masses during long integration periods, most likely due to strong mixing across the North Atlantic ridge topography, as diagnosed by Roberts et al. (1996) in their experiments using a version of the GFDL model. In the MICOM results reported by CSBB, however, the dense water present in the buffer zones was advected into the interior with its characteristics preserved. Consequently, both the strength of the meridional overturning and the magnitude of northward heat transport were greater in MICOM than in the depth-coordinate GFDL/CME model results.

In this work, we extend the study of CSBB by presenting the results of sensitivity experiments for MICOM in configurations similar to those of the aforementioned GFDL/CME studies. Our focus is on characterizing the transformation of water masses in each model case and on tracking the pathways from the northern boundary region into the interior, to determine, in particular, the dependence of these processes on northern buffer zone parameters and on model grid resolution. Comparison of our results to those of the GFDL/CME model studies and to observations will illustrate the inherent characteristics of the density-coordinate formulation and will also indicate the modifications needed to improve the model's ability to simulate the three-dimensional North Atlantic circulation. This work is part of the CME, a multiyear, multi-institutional series of model applications and analyses with the goal of establishing a sequence of baseline calculations of the wind- and thermohaline-driven large-scale ocean circulation (Bryan and Holland 1989; Döscher et al. 1994; Böning et al. 1995; BBHD; CSBB). Important component activities of this effort include the design and execution of the benchmark simulations, analysis of the results, and comparison with observations (U.S. WOCE Office 1993).

The paper is organized as follows: The numerical model and the configuration of the experiments are described in section 2. The observed water mass transformations in the northern North Atlantic are reviewed in section 3 for the purpose of comparison to the model results. In section 4, we examine the time evolution of the water mass volumes in the model experiments, the key time-averaged quantities of meridional overturning

strength and heat transport, the North Atlantic water mass transformation rates simulated in the various experiments, and the subsequent pathways of modified water into the model interior basin. Among the tools developed for this analysis are three-dimensional mass transport budgets within specified density classes and diagrams that track the spread of a passive tracer indicative of water mass modifications. The results are summarized and discussed in the concluding section.

2. The model configuration and design of the experiments

For a review of the isopycnic coordinate model MICOM, the reader is referred to Bleck and Chassignet (1994). The present computational domain is identical to that of the GFDL/CME experiments and the experiments of CSBB, namely the North and equatorial Atlantic basin from 15°S to 65°N , including the Caribbean Sea and the Gulf of Mexico but excluding the Mediterranean Sea. The bottom topography is derived from a digital terrain dataset with $5'$ lat \times $5'$ long resolution (ETOPO5). A Kraus–Turner mixed layer parameterization is included. All surface boundary conditions are based on monthly climatological datasets. The wind stress and wind work values are taken from the Hellerman and Rosenstein (1983) climatology. The surface thermal boundary conditions are specified by a linear bulk formula described by Han (1984) while those for freshwater flux are implemented as a linear relaxation of surface salinity toward the Levitus (1982) climatology.

Open ocean boundaries are treated as closed, but are outfitted with buffer zones in which temperature and salinity are linearly relaxed, on the same timescale, toward the Levitus (1982) monthly climatological values. In addition to the northern and southern boundaries, buffer zones are located in the Gulf of Cádiz (representing the Mediterranean Sea outflow) and in the northwestern corner of the basin (on the Labrador shelf). In the absence of an ice model, relaxation in the latter zone prohibits intense winter cooling in the shelf region west of the Labrador Sea from producing unrealistically cold temperatures in the model results. The restoring timescale for the northern and southern buffer zones, regardless of their latitudinal extent, linearly decreases from 25 days at the inner edge to 5 days at the walls. The timescale for the Labrador shelf region is 25 days, and for the Gulf of Cádiz, 1 year.

The model equations are solved on a C grid forming a square mesh on a Mercator projection, with horizontal grid resolution for the various experiments as specified below. In the vertical, the 16 model layers include a variable-density mixed layer and 15 isopycnic layers with potential density (σ_θ) values and water mass characteristics as shown in Table 1. The mixing coefficients are given in Table 2 and are defined as A_{MH} (horizontal) and A_{MV} (vertical) for the momentum equations and A_{DH}

TABLE 1. Density and water mass characteristics of the interior isopycnal layers.

Layer	σ_θ	Water mass characteristics (Schmitz 1996)
2	24.70	
3	25.28	
4	25.77	upper
5	26.18	
6	26.52	
7	26.80	
8	27.03	upper intermediate
9	27.22	
10	27.38	lower intermediate
11	27.52	
12	27.64	
13	27.74	upper deep
14	27.82	
15	27.88	lower deep
16	27.92	

(horizontal) and A_{DV} (vertical) for the temperature and salinity equations.

The experiments are as follows.

- Experiment MW (medium resolution, wide buffer zones): Base experiment, identical to MIAMI-1 in CSBB. Horizontal grid resolution 0.9° long. Width of northern and southern buffer zones $\sim 4^\circ$. (Comparable to GFDL/CME expt N1-26.0; Böning et al. 1995.)
- Experiment MN (medium resolution, narrow buffer zones): As MW but with buffer zones of width $\sim \frac{1}{3}^\circ$.
- Experiment HW (high resolution, wide buffer zones): Horizontal grid resolution $\frac{1}{3}^\circ$ longitude. Width of northern and southern buffer zones $\sim 4^\circ$.
- Experiment HN (high resolution, narrow buffer zones): As HW but with buffer zones of width $\sim \frac{1}{3}^\circ$. (Comparable to GFDL-CME expt N13-1; Bryan and Holland 1989.)
- Experiment MWM (medium resolution, wide buffer zones, modified temperature and salinity in northern buffer zone): As MW but with relaxation based on a hydrographic section in the Denmark Strait region of the northern restoring zone, following Döscher et al. (1994).

Experiments MW and HW were initialized with temperature and salinity for January from Levitus (1982), and likewise for MWM except for the modification in the Denmark Strait region of the northern buffer zone. The narrow-zone cases MN and HN were initialized from the year 10 solution of the corresponding wide-

zone model runs, in order to illustrate the divergence between wide-zone and narrow-zone results following model spinup, and were then integrated for 10 years to year 20. A passive tracer option was implemented in each experiment in year 21, and the model runs were continued for 5 years (10 years for MW).

3. Water mass transformations in the North Atlantic: Observational background

The model results will be evaluated by comparison to observational summaries of the transformation of warm North Atlantic waters to colder and denser water masses. Schmitz and McCartney (1993) and Schmitz (1996) present comprehensive views of these progressive transformations, beginning with an estimated 13 Sv of upper-layer water (warmer than 7°C) entering the subpolar gyre through the North Atlantic Current (NAC) system, north of $\sim 40^\circ\text{N}$. Branches of this flow reach the GIN seas through the Faroe Channel, the Iceland-Scotland ridge, and the Denmark Strait, where cooling creates dense water masses that return to the gyre as overflows across the GIS ridge system. The waters formed to the east of Iceland combine and flow to the southwest, passing through the Charlie-Gibbs Fracture Zone (CGFZ) and eventually encountering and mixing with the Denmark Strait overflow. The ~ 5 Sv thus formed below the GIS ridge system, together with ~ 4 Sv of entrained lighter waters, join a deep northern boundary current (DNBC) that flows from east to west below the subpolar ridges and islands, carrying ~ 16 Sv of overflow water, entrained upper-layer water, recirculating Labrador Sea Water (LSW), and upwelled AABW around Cape Farewell at the southern tip of Greenland. The DNBC flows toward the Labrador Basin, where open ocean deep convection forms ~ 4 Sv of LSW (Clarke and Gascard 1983), which are ultimately carried south within the DWBC at the level of upper NADW. The Schmitz and McCartney (1993) scenario culminates in an export from the subpolar gyre, within the DWBC, of 16 Sv of NADW from three sources: the dense overflows and entrained upper-layer water, which contribute 9 Sv of lower NADW (depth ~ 2500 m, $T = 1.8^\circ\text{--}3.0^\circ\text{C}$, $\sigma_\theta \approx 27.8\text{--}27.9$); the LSW, which contributes 4 Sv to the DWBC as upper NADW (depth ~ 1500 m, $T = 3.0^\circ\text{--}4.0^\circ\text{C}$, $\sigma_\theta \approx 27.76\text{--}27.78$); and 3 Sv of AABW that upwell at midlatitudes, reaching the subpolar gyre to circulate in the DNBC before returning to the south.

The water from the Labrador Sea exported to the south within the DWBC as upper NADW ($T = 3.0^\circ\text{--}$

TABLE 2. Parameters of the experiments. For all experiments, the quadratic bottom drag coefficient is 1.3×10^{-3} .

Experiment	A_{MH} ($\text{m}^2 \text{s}^{-1}$)	A_{MV} ($\text{m}^2 \text{s}^{-1}$)	A_{DH} ($\text{m}^2 \text{s}^{-1}$)	A_{DV} ($\text{m}^2 \text{s}^{-1}$)
MW, MN, MWM	1×10^4	0	2×10^3	3×10^{-5}
HW, HN	5×10^2	0	4×10^2	3×10^{-5}

4.0°C) is formed in winter (with considerable interannual variability) in the central Labrador Sea, a cyclonic gyre of scale 200–400 km centered near 56°–57°N, 53°–56°W (Clarke and Gascard 1983). The formation process begins as the East and West Greenland Currents transport near-surface freshwater and a deeper core of relatively warm, salty Irminger Basin water into the Labrador Sea. The West Greenland current flows across the northern end of the Labrador Basin and combines with waters of polar origin to form the Labrador Current, which continually freshens the surface waters of the gyre. Intense winter cooling by Arctic air masses strengthens the cyclonic circulation in the region, bringing about doming isotherms in gyre center, reduced stratification, and convective overturning that mixes the fresh, cold surface waters downward. From the Labrador Sea, LSW is advected toward the equator within the DWBC, and northeastward into the Irminger Basin, from where it recirculates within the DNBC. The process by which newly formed LSW migrates from the central Labrador Basin into the DWBC is not fully understood; the new water may recirculate in the gyre for some time before progressing to the south (Pickart 1992). The LSW can be tracked by its characteristic low potential vorticity signature within the DWBC as far south as Cape Hatteras, where it crosses under the Gulf Stream (Talley and McCartney 1982).

In addition to the LSW and the dense overflows, a third, relatively warm ($T = 4.0^{\circ}\text{--}5.0^{\circ}\text{C}$) water type has been identified within the DWBC, lying above the upper and lower NADW cores (depth $\sim 700\text{--}1000$ m). Traced to low northern latitudes by its high CFC (F-11) concentration (Fine and Molinari 1988), it was initially believed to be a variant of LSW produced in warmer winters. However, Pickart (1992) identifies this water mass as having been formed in the southern Labrador Sea inshore of the NAC, characterized both by the anomalously fresh salinity of that region and by more consistent ventilation than the upper NADW.

4. Water mass transformations in the North Atlantic: Model results

The water mass transformations simulated in the numerical experiments (defined in section 2) are documented by methods that focus on the time evolution of water mass volumes in each experiment and on time-averaged quantities for the final years of the model integrations.

a. Time evolution of water masses

We first examine the impact of horizontal grid resolution and width of the buffer zones on the evolution of the water mass volumes by monitoring in time the amount of mass present in each layer for each of the model experiments. The time evolution (years 1 through 25) of the domain-averaged layer thicknesses for the

mixed layer and the 15 isopycnal layers is presented in Fig. 1 for the first four experiments introduced in section 2 (MW, MN, HW, and HN). When multiplied by the domain area, the averaged layer thickness represents the volume of water of density corresponding to each isopycnal layer. Only the September averaged layer thicknesses are plotted in order to remove the seasonal signal. The bottom curve in each panel of Fig. 1 shows the time evolution of the heat content, defined as

$$\rho c_p \sum Th \Delta x^2 / \sum \Delta x^2 \quad (\text{units J m}^{-2}), \quad (1)$$

where $\rho = 1000 \text{ kg m}^{-3}$, $c_p = 3990 \text{ J kg}^{-1} \text{ K}^{-1}$, T is temperature, h is layer thickness, Δx is horizontal grid size, and the sums are taken over all horizontal grid points in all layers. With the exception of experiment HW (Fig. 1c), the solutions have not approached thermal equilibrium by the end of the 25-yr period.

The temporal changes in basin-averaged layer thickness that are apparent in Fig. 1 can occur through mixed layer entrainment/detrainment processes, through the relaxation to climatology that simulates water mass production outside the model domain, and, to a lesser extent, through diapycnal mixing between interior model layers. For the upper, wind-driven layers (layers 1–8 in Fig. 1), the changes in layer volume are relatively steady over time, while the deep circulation continues to evolve in the four experiments. These changes in deep-layer volume are associated with the renewal of dense water as the thermohaline circulation adjusts to the forcing, a process that will occur on a scale of hundreds of years. For the medium- and high-resolution runs with wide buffer zones (MW and HW, respectively), the temporal changes in volume for the deep layers are similar. In both cases (Figs. 1a,c), but more noticeably in MW (Fig. 1a), layers 13 and 16 lose mass, principally to the benefit of the middle layers (9–12). The behavior of the medium-resolution, narrow-zone MN (Fig. 1b) is similar to that of its wide-buffer-zone counterpart MW (Fig. 1a), although MN displays a more pronounced loss of mass in layer 15 (and gain in 14). In the narrow-zone high-resolution experiment HN (Fig. 1d), however, a rapid loss of mass from layer 16 results in a near-equivalent gain by layer 15, in contrast to the more even transfer of lost layer 16 mass to layers above that is seen in HW (Fig. 1c).

The similarity noted above in basin-averaged layer thickness changes between experiments MW and HW (Figs. 1a,c), or between MW and MN (Figs. 1a,b), conceals the fact that changes over time in the geographical distribution of mass within a given layer may depend upon the choice of model grid spacing or buffer zone width. Such changes can occur when a layer gains or loses mass through the processes described above, or when layer interfaces deform as the circulation evolves. Focusing on the basin-averaged volume evolution for the three deep-water layers (14, 15, 16) in Fig. 1, we note that layer 15 ($\sigma_{\theta} = 27.88$) exhibits the widest range

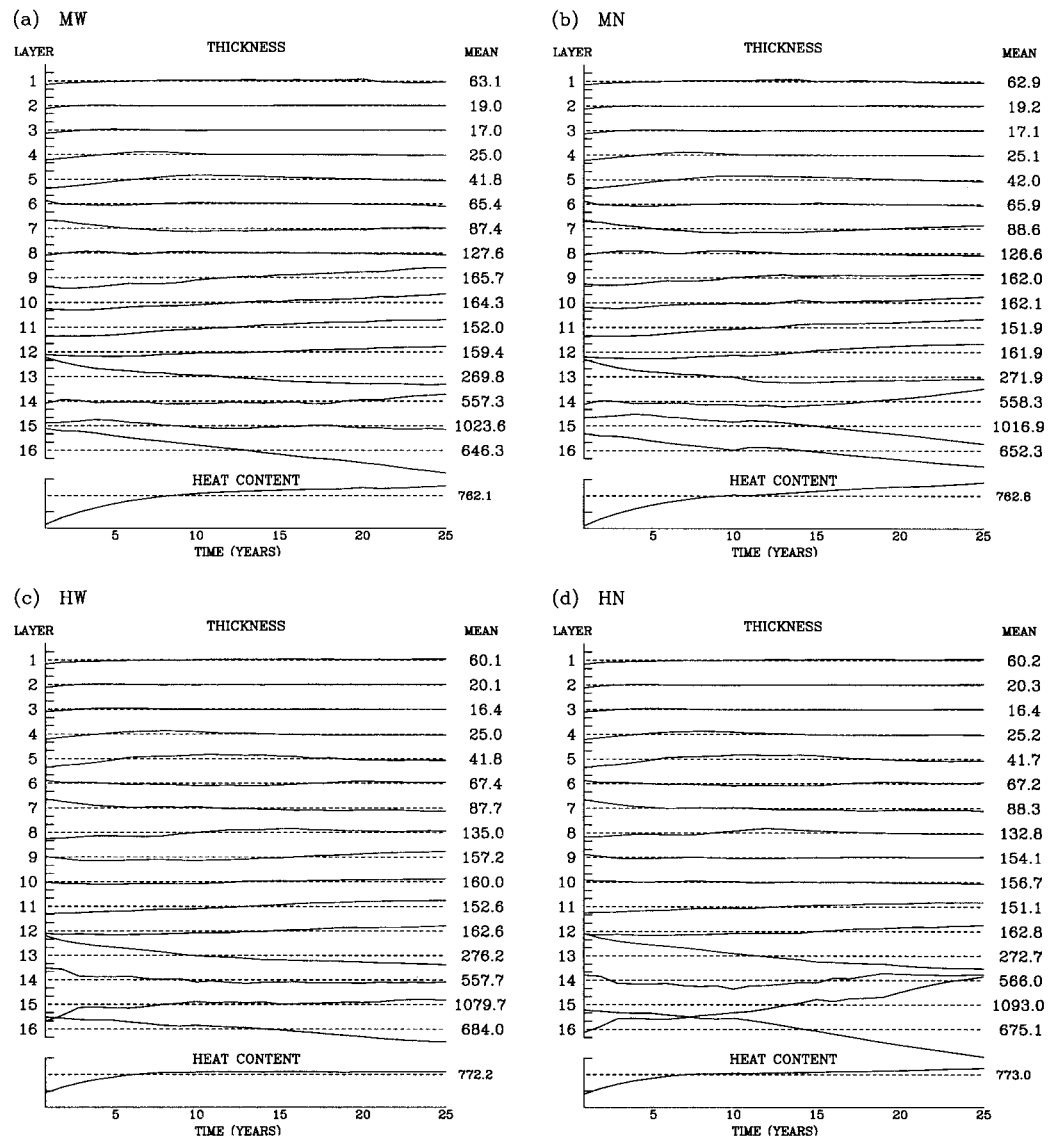


FIG. 1. Twenty-five-year time evolution of the domain-averaged layer thicknesses in meters (mixed layer and 15 isopycnal layers), and of the domain-averaged heat content (bottom curve), computed for Sep for (a) expt MW, (b) expt MN, (c) expt HW, (d) expt HN. Time-mean values shown at right. Tick marks on left axis indicate ± 10 m relative to time-mean value.

of differences in that evolution among the four experiments—relatively steady in MW and HW, losing mass in MN, and gaining mass in HN. We therefore choose that layer to illustrate in Fig. 2 the basinwide changes in layer thickness (though not the time evolution of those changes) that have taken place between September of model year 11 and September of year 25. Year 11 marks the first year of integration of the narrow-zone experiments MN and HN following their initiation from the respective wide-zone model results, and is also a sufficiently late time in the simulation for the surface mechanical spinup to have been achieved; the month of September is chosen because the mixed layer is shallow at that time.

Although the domain-averaged layer 15 thickness remains relatively steady during the final 15 years of the wide-zone integrations MW and HW (Figs. 1a,c), the contours of layer thickness difference over time (Figs. 2a,c) reveal the redistribution of mass within the layer that has occurred in both experiments. Along the western boundary of the subtropical gyre, layer 15 thins as the isopycnals slope downward (somewhat more steeply in the high-resolution HW) to accommodate development of the model DWBC. In the subpolar gyre, close to the northern relaxation region of the model, a sharper gradient of layer thickness difference can be seen for the high-resolution experiment HW (Fig. 2c) than for the medium-resolution MW (Fig. 2a), indicating stron-

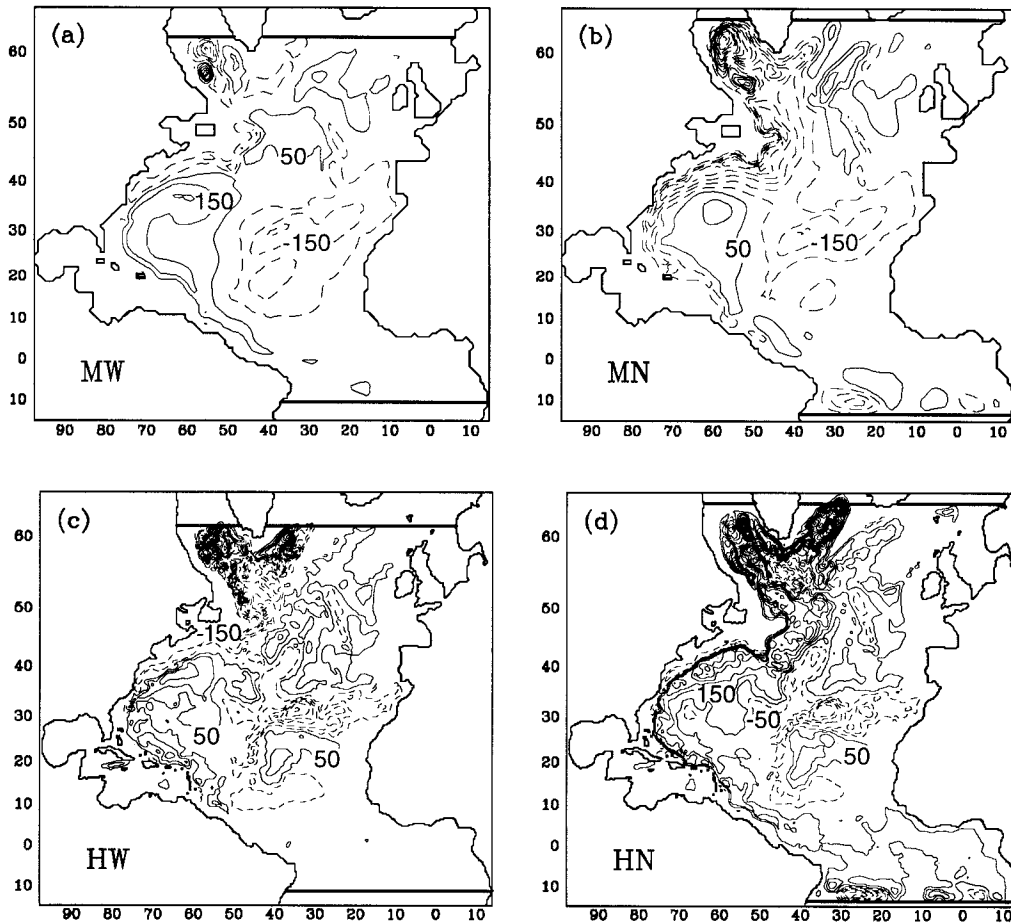


FIG. 2. September year 25 minus September year 11 thickness (m) of layer 15 ($\sigma_\theta = 27.88$). Contour interval 100 m. Dashed lines denote negative values; the zero contour is not shown. Heavy horizontal lines indicate extent of buffer zones. (a) Expt MW, (b) expt MN, (c) expt HW, and (d) expt HN.

ger buffer zone conversions to dense water in the high-resolution case. These conversions are reflected in the increase in basin-averaged layer 15 thickness for experiment HW seen in Fig. 1c. In the eastern basin west of the Gulf of Cádiz, layer 15 thins (while layer 16 thickens) over the 15-yr period in both MW and HW (Figs. 2a,c). Experiments with the DYNAMO (1997) analog to HW also indicate an input of mass to layer 16 in this region, compensating for a loss of layer 16 mass (due to relaxation at the southern boundary) while simultaneously allowing the Gulf of Cádiz relaxation to maintain the layer interface heights prescribed by climatology (Y. Jia 1998, personal communication).

Comparison of Figs. 1b,d to Figs. 1a,c indicates the effect of narrower buffer zones on the time evolution of the domain-averaged lower-layer volumes. In the medium-resolution MN, layer 15 loses mass over the period from year 11 to year 25 (Fig. 1b), primarily in the region of the DWBC and in the western lobe of the subpolar gyre (Fig. 2b). The narrower buffer zone in this experiment is less effective in renewing the deep water mass of layer 15 than the wide zone of experiment MW, in

which significantly less thinning of the layer occurs along the western boundary (Fig. 2a). In the high-resolution HN, however, layer 15 gains mass, principally in the subpolar gyre region (Fig. 2d). It is in layer 16 of HN (Fig. 1d) that most of the reduction in deep water mass formation appears to take place, due to the inability of the narrow buffer zone to renew the densest water mass in the model domain.

Both the time evolution of basin-averaged layer volumes and the changes in layer 15 mass distribution over time indicate a progression of deep-water formation processes through the various experiments. The loss of mass in layer 15 in experiment MN (Figs. 1b, 2b), with narrow buffer zones, becomes insignificant in the same layer of MW (Figs. 1a, 2a), as the wider buffer zones more efficiently accomplish the renewal of deep water. The change in grid resolution for experiment HN results in a basin-averaged increase in layer 15 thickness (Figs. 1d, 2d), but a significant loss in layer 16 (Fig. 1d), as the narrow buffer zones fail to bring about conversion of water to the densest layer in the model vertical structure. The most stable configuration among the four ex-

periments for the deep-water layers 14–16 during the final 5 years of the integration is seen in Fig. 1c for the wide-zone high-resolution experiment HW, with strong conversions to dense water occurring in the subpolar gyre region of layer 15 (Fig. 2c).

In order to further examine the time evolution of water mass conversions in the model results, a passive tracer was introduced in all experiments beginning at year 21 and the model runs were continued for 5 years (10 years for MW). The tracer was designed to tag water that is added to an isopycnal layer by the relaxation of layer interface depths to climatology within the buffer zones. Specifically, if h_k is the thickness of model layer k , and if δh is the increase in thickness experienced by layer k during the relaxation process, then

$$\text{tracer}_k^{\text{new}} = (h_k \times \text{tracer}_k^{\text{old}} + \delta h)/(h_k + \delta h). \quad (2)$$

Note that tracer values are expressed as concentration, varying between the initial value of 0 and the maximum possible value of 1. The water mass of thickness δh , that is, the water newly added to layer k , is assumed to be saturated with tracer so that the concentration of tracer indicates the extent of water mass modifications that have taken place. When tracer concentration is multiplied by layer thickness, the product indicates the volume of tagged water in each layer. The tracer option also allows the tagged water to be followed as it is advected into the interior.

Figures 3a,b,c show tracer concentration multiplied by layer thickness, in units of meters, for layer 15 ($\sigma_\theta = 27.88$) for the annual mean of years 21, 25, and 30, respectively, of experiment MW. In comparison to the limited extent of water mass spreading for the initial year of tracer injection (Fig. 3a), the pattern for year 25 (Fig. 3b) shows that the layer 15 water formed in the northern buffer zone has been swept around the subpolar gyre and down the western boundary to $\sim 40^\circ\text{N}$. East of Iceland, the converted water has been advected into the deeper ocean around the Reykjanes Ridge. Advection into the interior from the Gulf of Cádiz is also apparent. After 10 years of tracer injection in MW (Fig. 3c), the dense water that has undergone conversion in the buffer zone east of Iceland passes through the CGFZ, joins the flow from the boundary regions east and west of Greenland, and continues southward to the Antilles within the model DWBC. A recent analysis of North Atlantic chlorofluorocarbon (CFC) and hydrographic data by Smethie et al. (1999) indicates an approximate 20-yr transit time for lower NADW from its subpolar source region to $\sim 25^\circ\text{N}$. However, entrainment of older water during formation, as well as mixing along the southward path, may bias the CFC measurements to older ages, implying a somewhat shorter effective transit time of ~ 15 yr from high-latitude deep-water sources to the Antilles.

For the remaining three model experiments (HW, MN, HN), we show tracer concentration multiplied by layer thickness for layer 15 for the annual mean of year 25

only, the fifth year of tracer injection (Figs. 3d,e,f). The high grid resolution of experiment HW (Fig. 3d) is apparent in the more detailed patterns of the spread of tracer-injected water, as compared to those of the medium-resolution MW (Fig. 3b). By year 25 in HW, the tagged water has been advected to a point south of 25°N (as opposed to 40°N in MW) in a well-defined DWBC. Similar remarks apply in comparing the tracer patterns for the two narrow-zone cases with different grid resolutions, MN (Fig. 3e) and HN (Fig. 3f). The high-resolution simulations, with $\frac{1}{3}^\circ$ grid size, are inherently more inertial than those with grid size nearly three times as large, and they are less viscous as well (Table 2), leading to farther-reaching (though more narrowly delineated) DWBCs than in the medium-resolution results.

When the tracer diagrams are compared for pairs of experiments having the same grid resolution, however, the figures indicate that buffer zone width does not substantially affect the southward extent of the model DWBC. However, the truncated tongues of converted water evident in HN from 30° to 40°N (Fig. 3f vs Fig. 3d for HW) and in MN near 40°N (Fig. 3e vs Fig. 3b for MW) are evidence of the less effective renewal of deep water masses that takes place in the model runs with narrow conversion regions. Note that in experiment HN, the mass gain that occurs over time in the subpolar gyre region of layer 15 (Fig. 2d) is reflected in the broader pattern of tracer-injected water seen to the west of Greenland in Fig. 3f, as compared to the subpolar region loss of mass in MN, evident both in Fig. 2b and Fig. 3e.

b. Meridional overturning circulation and associated heat flux

The water mass transformations discussed in the previous section drive the meridional overturning circulation observed in the model experiments. The annual mean meridional overturning streamfunctions for year 25 of experiments MW, MN, HW, and HN are displayed in Fig. 4, and the corresponding curves for total heat transport, as well as for that part of the total transport due to the gyre component of the overturning, are shown in Fig. 5. The maximum overturning rate for the four cases ranges from 17 to 23 Sv, in reasonable agreement with observational estimates (Schmitz and McCartney 1993; Schmitz 1995). In Fig. 4, we observe first that for a given resolution, the experiments with wide buffer zones exhibit stronger transports (by ~ 2 Sv) than their counterpart experiments with narrow buffer zones, and second that for a given buffer zone width, the high-resolution experiments exhibit stronger transports than their counterpart experiments with medium resolution (by ~ 4 Sv). Note that the larger maximum overturning of experiment HN (21 Sv) in comparison to that of MW (19 Sv) is in contrast to the BBHD finding of smaller overturning rates in high-resolution, narrow-buffer-zone GFDL/CME simulations. Similarly, the Beckmann et al.

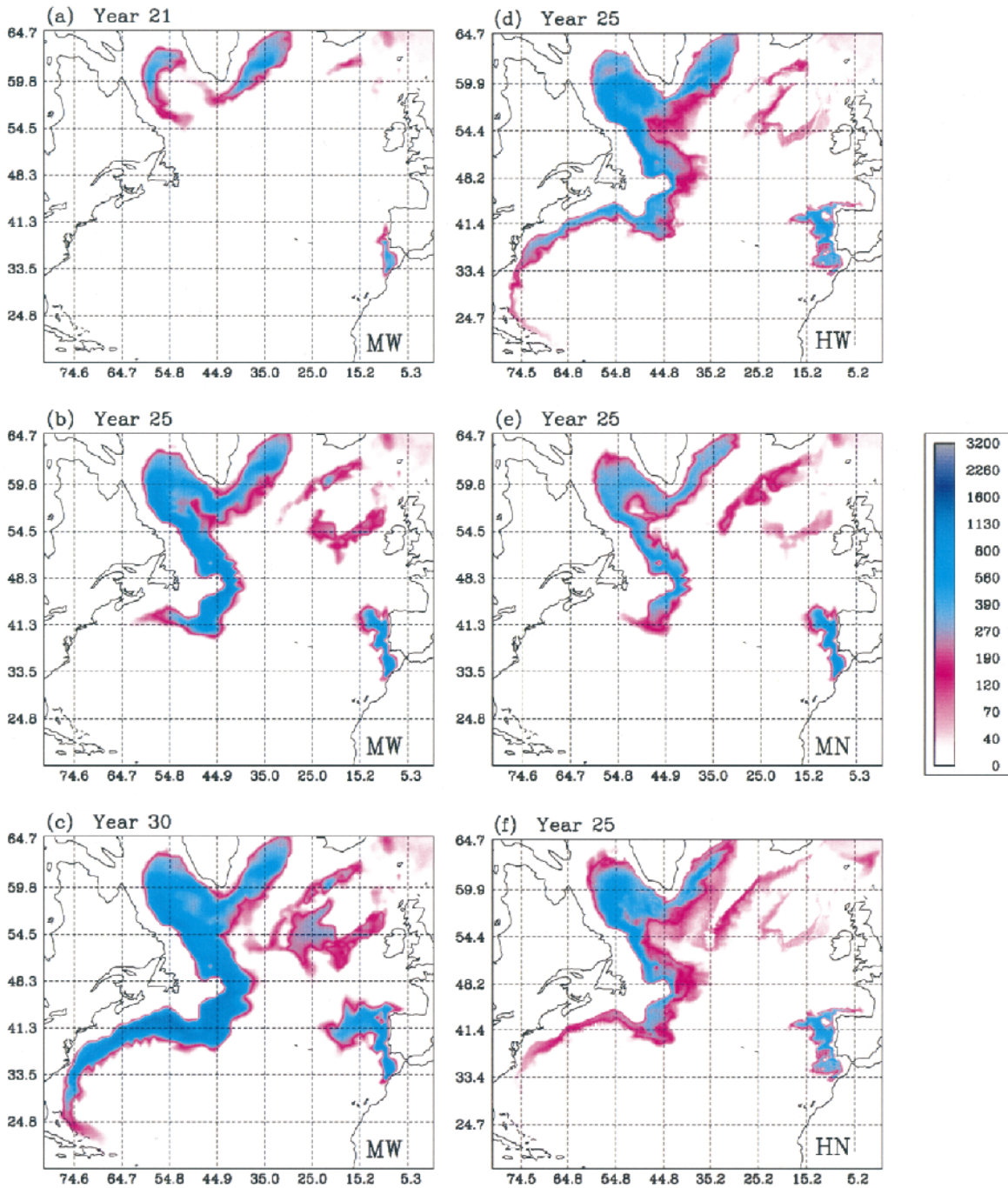


FIG. 3. Tracer concentration times layer thickness (m) for layer 15 ($\sigma_\theta = 27.88$). (a) Expt MW, yr 21; (b) expt MW, yr 25; (c) expt MW, yr 30; (d) expt HW, yr 25; (e) expt MN, yr 25; (f) expt HN, yr 25.

(1994) observation of decreasing meridional overturning rates with increasing horizontal resolution, when buffer zone width is held constant, is not seen in the present experiments.

The quasi-linear correspondence between the intensity of the annual mean overturning circulation and the maximum northward transport of heat, first noted by BBHD, is also indicated for our model results by com-

parison of Figs. 4 and 5. At 25°–30°N, the latter figure shows annual mean northward total heat transport values ranging from 1.0 PW for MN (1 PW $\equiv 10^{15}$ W) to 1.3 PW for HW, consistent both with the 1.2 PW estimated at 25°N by Hall and Bryden (1982) and with the 1.1 PW indicated at 30°N by the inverse calculation of Macdonald and Wunsch (1996). For our high-resolution cases, the maximum annual mean value (1.4 PW for HW)

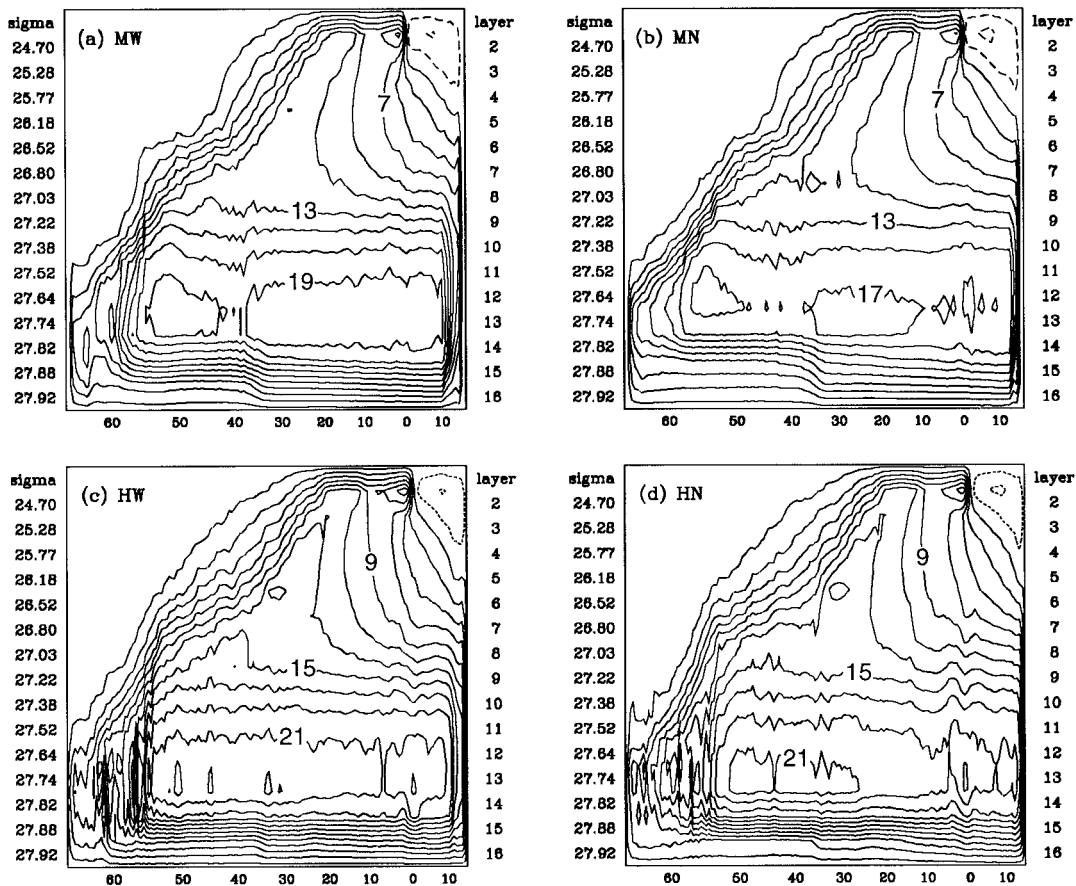


FIG. 4. Annual mean meridional overturning streamfunction, year 25, for (a) expt MW, (b) expt MN, (c) expt HW, and (d) expt HN. Contour interval 2 Sv. The zero contour is not shown. Vertical axes indicate σ_t and layer number for the 15 isopycnal layers.

occurs at $\sim 35^\circ\text{N}$, but falls nearer $\sim 20^\circ\text{N}$ for the medium-resolution runs (1.2 PW for MW). Heat transport values for the DYNAMO (1997) high-resolution ($1/3^\circ$) density-coordinate experiment reach a maximum of 1.2 PW in the range $20^\circ\text{--}25^\circ\text{N}$, but remain relatively high (~ 1.1 PW) at 35°N .

Böning and Herrmann (1994) note the dependence of annual mean heat transport values on model boundary conditions in their results from a $1/3^\circ$ GFDL/CME experiment with narrow (4-gridpoint) buffer zones. That experiment produced a maximum meridional overturning rate of 12 Sv, with a correspondingly low annual mean heat transport maximum of 0.65–0.75 PW located at $30^\circ\text{--}35^\circ\text{N}$. Our comparable experiment HN, however, shows 1.3 PW in that latitude range, and, analogous to the meridional overturning results, both HW and HN produce greater annual mean total heat transport values than the medium-resolution cases MW and MN (Fig. 5). This is in contrast to the results of Holland and Bryan (1994) for 1° , $1/3^\circ$, and $1/6^\circ$ GFDL/CME experiments, which indicated similar heat transport values for all resolutions when similar boundary conditions were applied.

In Fig. 5, that part of the total heat transport due to the gyre component of the overturning, shown in the lower curves for the four experiments, is seen to be responsible for a significantly greater contribution to the total transport in the high-resolution runs HW and HN than in the medium-resolution MW and MN, north of $\sim 35^\circ\text{N}$. In contrast to the broad, diffuse boundary currents of the medium-resolution runs, the narrow, more inertial Gulf Stream–North Atlantic Current system of the high-resolution simulations is capable of advecting warm water of the subtropical gyre farther to the north and northeast with less diffusion of temperature, providing a larger gyre component contribution to the total heat transport and leading to the higher total transport exhibited by experiments HW and HN north of $\sim 35^\circ\text{N}$ (Fig. 5).

The experiments of Döscher et al. (1994) and Gerdes and Köberle (1995), carried out with grid spacing $1^\circ \times 1.2^\circ$, indicate that the meridional overturning circulation (and, correspondingly, the meridional heat transport) should reach a quasi-dynamic equilibrium in approximately 15 years. Based on those results, BBHD stated that a 20-yr integration time should be sufficient to reach

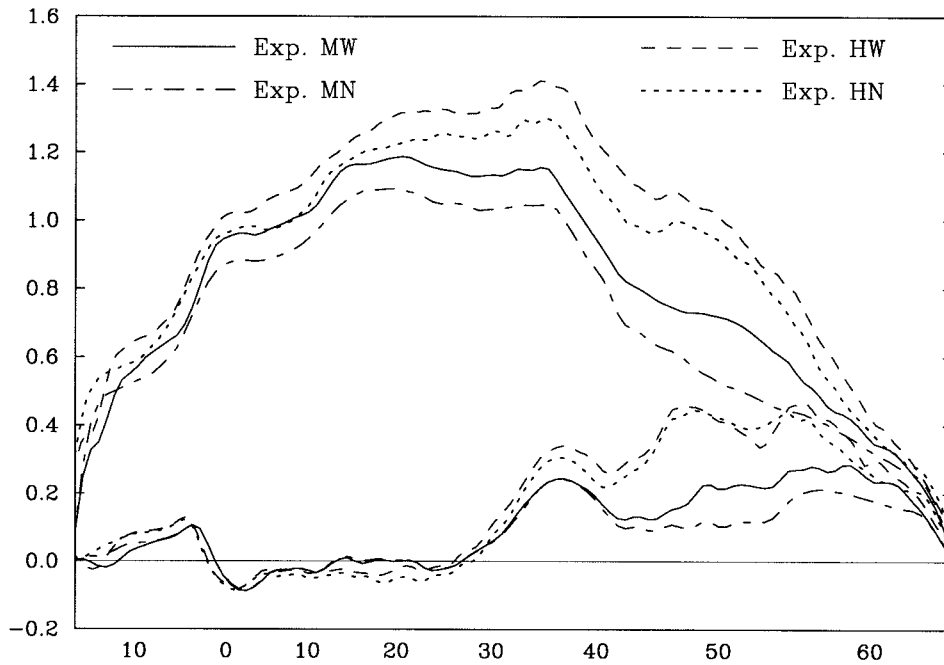


FIG. 5. Annual mean meridional heat transport (PW), year 25, for experiment MW, MN, HW, HN. Four upper curves: total heat transport. Four lower curves: heat transport due to the gyre component.

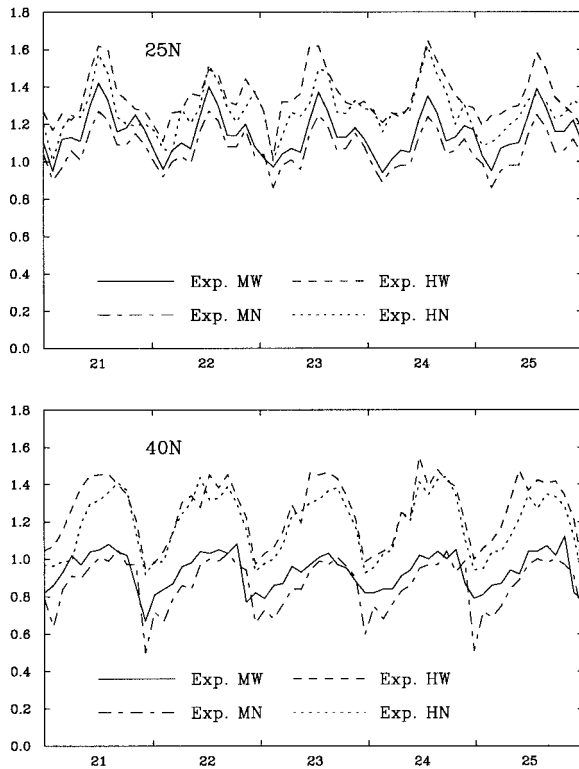


FIG. 6. Annual cycle of total meridional heat transport (PW) at 25°N and 40°N for expts MW, MN, HW, HN, years 21 through 25.

a similar equilibrium in higher-resolution runs as well. This supposition is confirmed for our experiments by the relative steadiness, over the last 5 years of each of the four model runs, of the annual meridional heat transport cycle at 25°N and at 40°N (Fig. 6). Once such an equilibrium has been achieved, it is not strongly modified by the long-term adjustment of deep-layer volume (discussed in sec. 4a), as can be shown by comparison of the annual mean overturning streamfunctions at 20 years for two of the experiments of CSBB, MIAMI-1 (i.e., expt MW) and MIAMI-4. In contrast to MIAMI-1, which was initialized from the Levitus (1982) climatology, the MIAMI-4 experiment was initialized from year 220 of an NCAR/CME simulation that exhibited a near-massless layer 16 at that time (see Fig. 14 of CSBB). In MIAMI-4, advection of dense water from the buffer zones into layer 16 has not brought about a steady state in the thickness of that layer after 20 years, and the southward deep flow near the southern boundary in the MIAMI-4 overturning streamfunction remains shallower than the analogous flow in MIAMI-1. Nonetheless, the year 20 streamfunction maximum is the same (19 Sv) in both experiments, indicating that the magnitude of the overturning circulation developed during the initial mechanical adjustment is relatively steady.

In the seasonal cycles of heat transport shown in Fig. 6, higher monthly transport values are seen at both latitudes for the high-resolution experiments HW and HN than for their medium-resolution counterparts MW and MN. However, the differences in month-by-month values between the two pairs of experiments are perceptibly

TABLE 3. Density classes for mass transport budgets.

	Class	Potential density	Model layers
1	(Upper)	$\sigma_\theta < 26.8$	2–6
2	(Upper intermediate)	$26.8 \leq \sigma_\theta \leq 27.0$	7–8
3	(Lower intermediate)	$27.0 < \sigma_\theta \leq 27.5$	9–11
4	(Upper deep)	$27.5 < \sigma_\theta \leq 27.8$	12–13
5	(Lower deep)	$\sigma_\theta > 27.8$	14–16

greater at 40°N than at 25°N, due to the greater contribution of the gyre component to the total transport of heat at the more northern latitude in the high-resolution results (Fig. 5). In their $\frac{1}{3}^\circ$ GFDL/CME experiment, Böning and Herrmann (1994) find that the magnitude of seasonal variations in heat transport is less sensitive to horizontal grid resolution in the subtropics than in the regime of the North Equatorial Countercurrent, where seasonal changes in heat content are large. Their study also finds that such variations are primarily a wind-driven effect in the subtropical North Atlantic, and thus not closely tied to the model boundary conditions. Our figures of the seasonal cycle of heat transport at 25°N and 40°N (Fig. 6) indicate that the seasonal variations are in phase among the four experiments, each of which shows the observed winter minimum and summer maximum in the subtropics (Hsuing et al. 1989; Molinari et al. 1990), and that the amplitude of the seasonal cycle is greater for the high-resolution experiments than for those of medium grid size. Given the relationship between seasonal variations in heat transport and wind-driven effects, the larger seasonal cycle amplitude exhibited by the high-resolution experiments is an expected manifestation of the more inertial character of those simulations. However, the yearly range between minimum and maximum heat transport values for the high-resolution case HW, ~ 0.5 PW at both latitudes shown in Fig. 6, is greater than the ~ 0.2 PW amplitude found at those locations by Böning and Herrmann (1994) in their $\frac{1}{3}^\circ$ experiment forced (as in our case) by the Hellerman and Rosenstein (1983) winds.

c. Box diagrams: Time-averaged transformations

The annual mean meridional overturning and associated transport of heat are products of the time evolution of water mass conversions in the model, which we now consider in detail by means of mass transport budgets. The budget calculations are based on a division of the model mixed layer and 15 isopycnal layers into five density classes, as in Schmitz's (1996) division for the global ocean (Table 3), and are carried out for 5-yr-mean model results in boxes $\sim 9^\circ$ longitude square. Within the box diagrams, we focus on that part of the model basin where, according to observations, the major North Atlantic conversions from warm to cold water

take place, namely from $\sim 40^\circ\text{N}$ to the northern model boundary at $\sim 65^\circ\text{N}$.

Transfers of mass between density classes occur primarily due to diabatic processes in the surface mixed layer and, to a lesser degree, through diapycnal mixing between waters of different density classes. An additional type of mass transfer between classes occurs in the model buffer zones. In the northern zone, for example, the relaxation to climatology simulates the production of dense water that occurs in reality outside the model domain. The denser (or lighter) water masses formed by these processes spread laterally along the path of boundary currents within the cyclonic subpolar gyre, eventually reaching the DWBC and joining in the large-scale overturning circulation of the Atlantic.

The reader is referred to the appendix for a detailed description of the budget computations.

1) THE BASE EXPERIMENT MW

The mass budget diagrams for density classes 1 through 4 for the MW results (mean, years 21–25) are shown in Fig. 7. Water in class 1 (Fig. 7a) lies completely within the mixed layer as far north as the outcrop line of $\sigma_\theta = 26.8$ (Fig. 8a), the upper-limit density for the class. North of 40°N, a net volume flux of ~ 14 Sv in class 1 is carried to the north within the NAC and is converted to denser class 2 water in an area extending along the most northward-reaching streamline of the mixed layer subtropical gyre (Fig. 8b). This conversion is accomplished as surface water is advected into a region north of the class 1 outcrop (Fig. 8a), where the mixed layer density is increased by air–sea interaction. The region of most intense transfer into class 2 coincides with the strongest NAC flow, near 51°N, 42°W, and exhibits small standard deviation (~ 1 Sv) around the 5-yr mean diapycnal flux values.

In class 2 ($26.8 \leq \sigma_\theta \leq 27.0$; Fig. 7b), the conversion to denser water takes place in similar fashion to that in class 1 but farther to the north. Approximately 13 Sv flowing to the north and east are converted to class 3 water north of 50°N, near the outer edge of the mixed layer subtropical gyre (Fig. 8b) where the 27.0 density contour lies at the surface (Fig. 8a). As in the previous class, the conversion is primarily accomplished as eastward advection by the NAC along the northern edge of the gyre (Fig. 8b) transports class 2 water into a region of higher surface density. Relatively large standard deviation values (~ 2 Sv) are found in the region of strongest transfer into class 3, north of 54.5°N and south of Greenland, and in the associated lateral fluxes from the south and east into that area. This variability arises from shifts in the position and strength of the NAC between 40°W and 45°W during the model years that are included in the 5-yr mean.

In the mean model results, water in class 3 ($27.0 < \sigma_\theta \leq 27.5$; Fig. 7c) is in contact with the atmosphere between the 27.0 density contour (Fig. 8a) and the 27.5

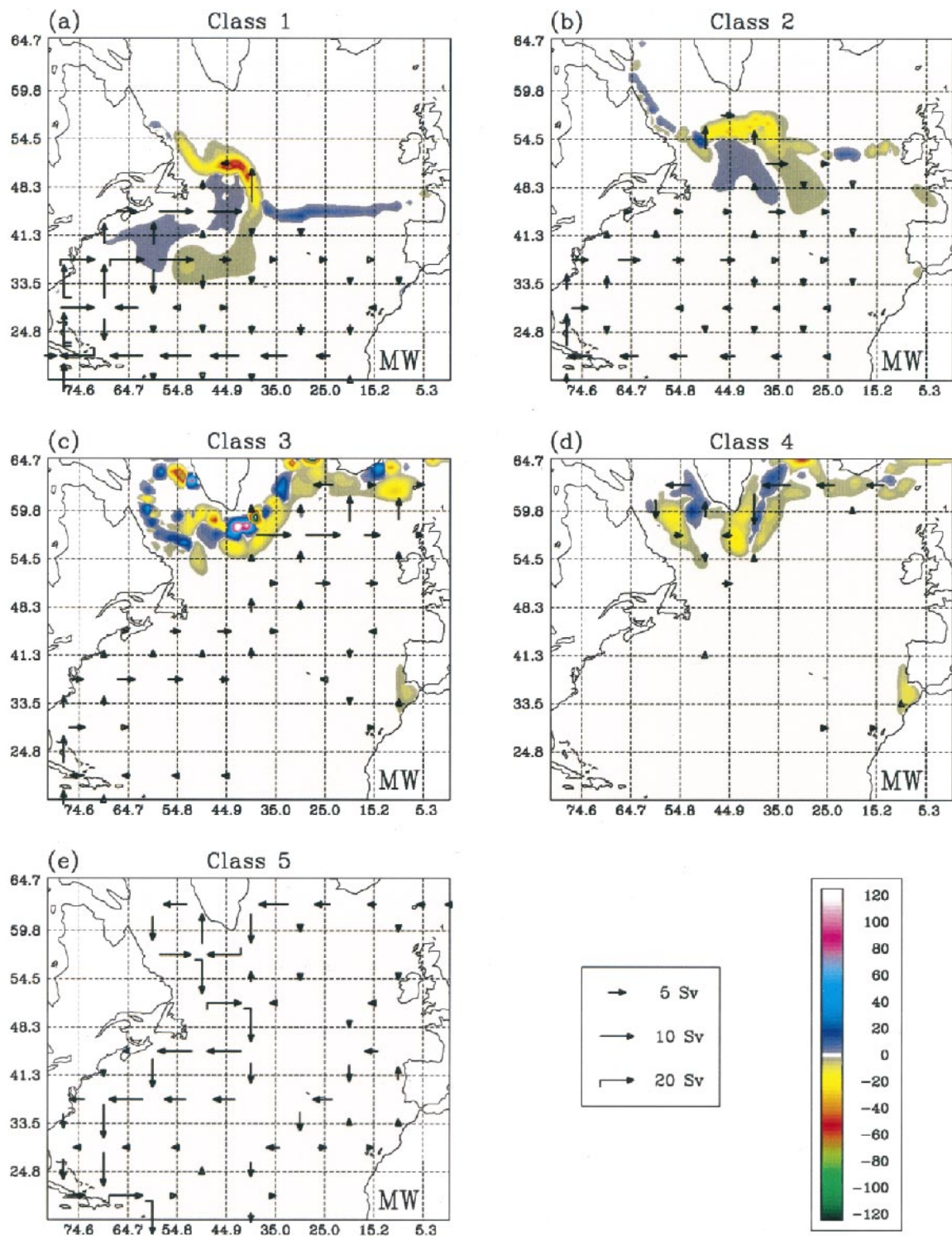


FIG. 7. Mass transport budget boxes for expt MW. (a) Class 1, (b) class 2, (c) class 3, (d) class 4, (e) class 5. Arrows denote intraclass fluxes (Sv). Colors indicate diapycnal fluxes (Sv) between the class being viewed and the next-heavier density class, with positive (negative) values indicating transfer into (out of) the class being viewed. See appendix for detailed explanation.

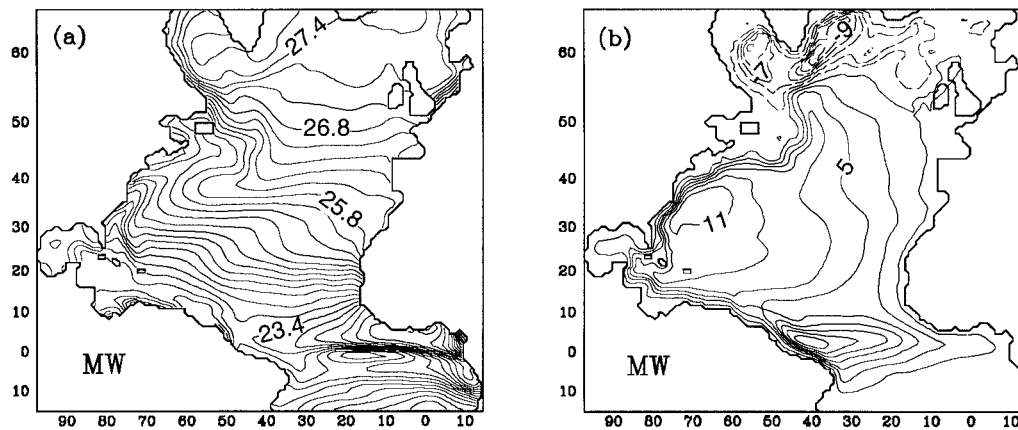


FIG. 8. (a) Mixed layer density (σ_θ), year 21–25 mean, expt MW. Contour interval $0.2 \sigma_\theta$ units. (b) Mixed layer streamfunction (nondivergent part; Sv), year 21–25 mean, expt MW. Contour interval 2 Sv. Dashed lines denote counterclockwise circulation; the zero contour is not shown.

contour, which roughly follows the outer edge of the mixed layer subpolar gyre (Fig. 8b). Within the northern buffer zone, strong transformations from class 3 into class 4 are apparent both to the east (8 Sv) and west (9 Sv) of Iceland, resulting from the relaxation to climatology that models the production of dense water in the GIN seas. Exchange of mass between class 3 and class 4 is evident in a diffuse area along the edge of the class 3 subpolar gyre. The strongest such interclass conversions appear to the southeast and southwest of Greenland, where high temporal variability exists both in the intersection of this class with the mixed layer and in the strength of the more intense lobe of the subpolar gyre, located south and east of Greenland (Fig. 8b). As in class 2, this variability is related to shifts in the position and strength of the NAC during the individual model years.

Class 4 ($27.5 < \sigma_\theta \leq 27.8$; Fig. 7d), in the 5-yr mean, includes mixed layer water around the southeastern and

southwestern coasts of Greenland and along the northern wall east of Greenland (Fig. 8a). Conversion of ~ 10 Sv to denser (class 5) water occurs in the model buffer zone east of Greenland, with the strongest transformation occurring in the Denmark Strait region between Greenland and Iceland. The remaining ~ 7 Sv that reached this density class from the class 3 buffer zone, together with ~ 1 Sv converted to class 4 south of the buffer zone and east of Greenland, flow into the Irminger Basin, around the southern tip of Greenland, and then into the Labrador Sea (Fig. 9a). Along this path, two regions of water mass transformation are apparent. First, ~ 5 Sv are converted from class 4 to class 5 in the Irminger Basin southeast of Greenland. Small standard deviations (< 1 Sv) are associated with this diapycnal transfer and with the mass fluxes from the south and north into that region. The class 4 westward flux around Cape Farewell, however, exhibits high variability related to changes in strength and position of the

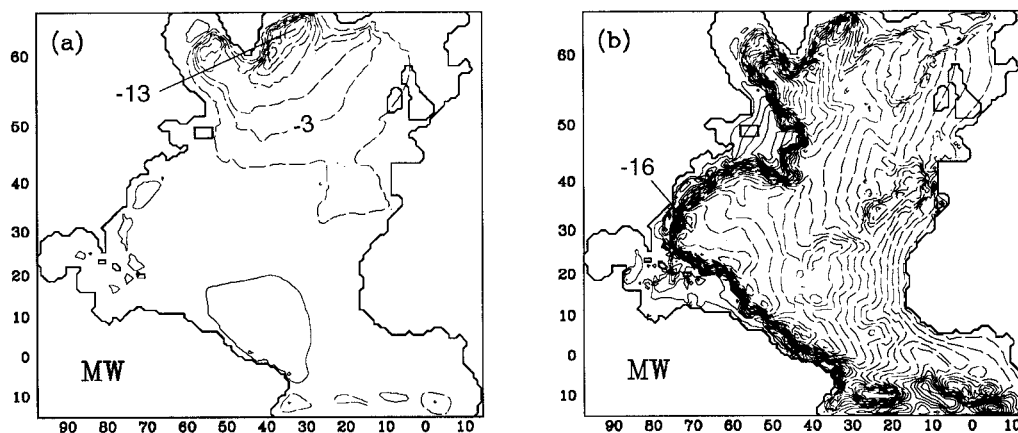


FIG. 9. (a) Class 4 streamfunction (nondivergent part; Sv), and (b) class 5 streamfunction (nondivergent part; Sv), for year 21–25 mean, expt MW. Contour interval 2 Sv for (a), 1 Sv for (b). Dashed lines denote counterclockwise circulation; the zero contour is not shown.

more intense lobe of the subpolar gyre for this class (Fig. 9a). The second region of water mass transformation apparent in class 4 is in the Labrador Sea, away from the model restoring zone. Here, ~ 3 Sv are converted to class 5 water in the model's representation of the open ocean convection that occurs in that basin (Clarke and Gascard 1983). The conversion to class 5 in the Irminger Basin takes place in a region where the mixed layer depth and subpolar gyre mass flux reach local maxima in March, the month of deepest winter mixing (Figs. 10a,b). In the deepest and densest part of the Labrador Sea, however (Figs. 10a,c), doming isopycnals bring about the upwelling seen to the west of Greenland (Fig. 7d), and the diapycnal transfer to class 5 is instead strongest on the western edge of the gyre, where the equatorward Labrador Current (Fig. 10b) drains LSW from the mixed layer into the DWBC.

Finally, in class 5 ($\sigma_\theta > 27.8$; Fig. 7e), the northern edge of the model subpolar gyre is marked by a deep cyclonic boundary current that carries more than 16 Sv from east to west around Cape Farewell, in good agreement with the observational estimate of Clarke (1984) for the deep-water transport around that point. The current continues into the southward-flowing model DWBC (Fig. 9b), which transports ~ 16 Sv across 48°N , with negligible standard deviation about the 5-yr mean. An additional ~ 2 Sv crosses that latitude in deep flow that originates in the buffer zone east of Iceland, giving a total southward transport of 18 Sv in class 5.

The scenario of water mass transformations in the MW results is one of stages of conversion from lighter to denser water, beginning with the advective transfers described above for class 1/class 2 and class 2/class 3. The ~ 13 Sv thus reaching class 3 is swept to the east and north with the large-scale subpolar gyre flow, into the model buffer zone east of Greenland, where the conversion to dense water that occurs north of the GIS ridge system is simulated. In class 3, a total of 18 Sv are converted into the denser class 4, with 10 Sv continuing to sink into class 5 while 8 Sv are carried within class 4 to the south, west, and north around Greenland. Along that path, the 8 Sv are converted into class 5 in the Irminger Basin (5 Sv) and in the Labrador Sea (3 Sv). The mass flux of ~ 18 Sv that finally reaches the densest class is then carried to the south with its density characteristics preserved (CSBB).

The observational summaries of Schmitz and McCartney (1993) and Schmitz (1996) indicate a total of 16 Sv carried southward across $\sim 48^\circ\text{N}$ within the DWBC, including 9 Sv lower NADW from the dense overflows and entrained upper-layer water, 4 Sv upper NADW from the Labrador Sea, and 3 Sv of AABW that upwells in midlatitudes and returns to the south. In comparison to these figures, the southward class 5 (lower deep) transport in MW; (a) omits 3 Sv of identifiable AABW upwelling into the density range of class 5; (b) includes 3 Sv of water from the Labrador Sea in the lower deep density range, but omits the contribution of

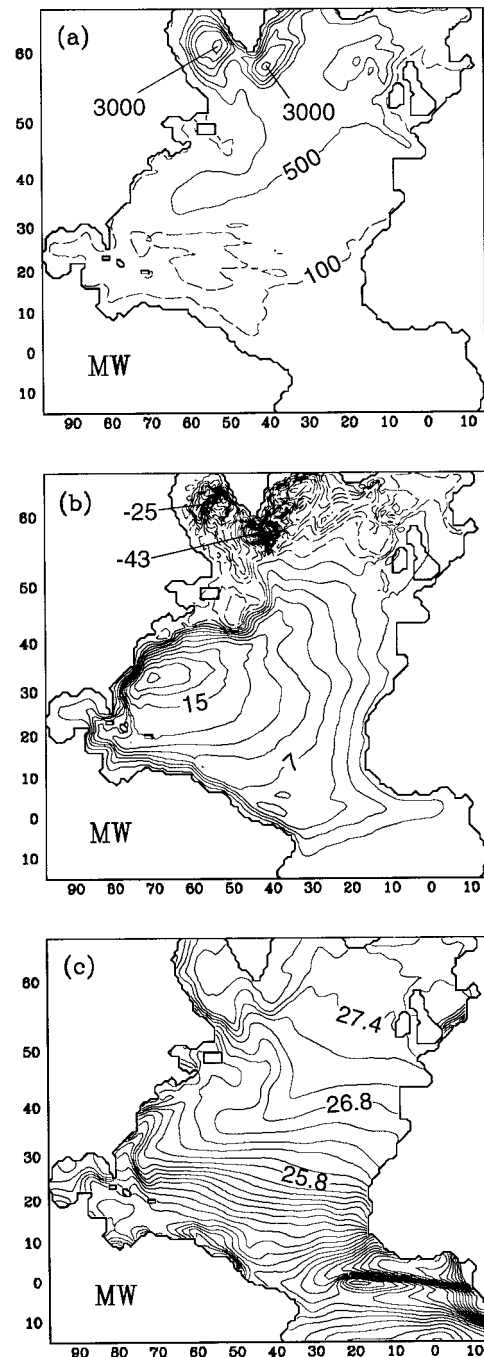


FIG. 10. (a) Mixed layer depth (m), (b) mixed layer streamfunction (nondivergent part; Sv), and (c) mixed layer density (σ_θ), for year 21–25 Mar average, expt MW. Contour interval 500 m for (a), 2 Sv for (b), $0.2 \sigma_\theta$ units for (c). Dashed lines in (b) denote counterclockwise circulation; the zero contour is not shown.

LSW to the upper NADW; (c) includes 5 Sv of deep water formed in the Irminger Basin, a formation region that is not specifically noted in observations; and (d) includes an additional 1 Sv of deep water produced in the northern buffer zone as compared to the amount

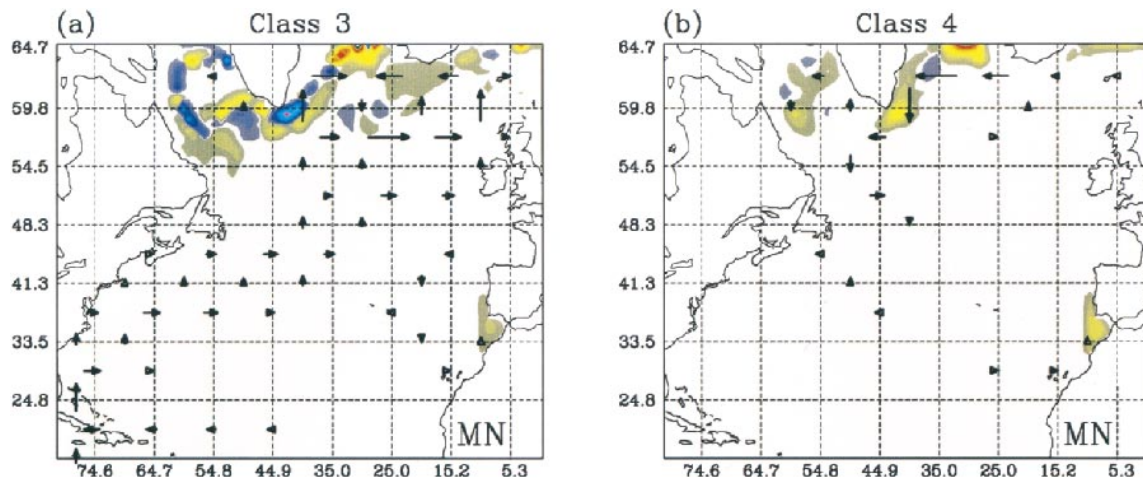


FIG. 11. As in Fig. 7 but for expt MN: (a) class 3, (b) class 4.

attributed to the real-world deep overflows and entrainment of upper-layer water.

The first of these differences, the absence from the MW results of a representation of the midlatitude AABW upwelling (McCartney 1993), is due to the use of σ_θ as the model vertical coordinate. Experiments in which σ_2 is used as the model representation of density (Sun 1997), and in which the effects of thermobaricity are incorporated, will be reported in a subsequent paper. Second, regarding the contributions from the Labrador Sea in MW, the experiment appears to form only lower NADW (class 5 water) in the Labrador region, where the simulated convective process takes place in the most dense part of the subpolar gyre mixed layer (Fig. 8a). The model vertical resolution is apparently insufficient to capture the narrow density range of upper NADW or to properly model the variety of water types (discussed in section 3) that come together to form the final convected mass. The third point of difference, the model formation of deep water in the Irminger Basin, will be discussed in section 4c(4). Finally, it must be noted that although relaxation to climatology within the buffer zones is intended to simulate not only the formation of dense water but also the process of entrainment within the overflows, no explicit parameterization of entrainment is presently incorporated in the model.

2) IMPACT OF THE BUFFER ZONE WIDTH AND RESOLUTION

The water mass conversions in classes 1 and 2 of experiment MN, with narrow buffer zones, differ little from those of the wide-zone MW and are not displayed. In class 3 of MN, however (Fig. 11a), a more concentrated region of conversion to dense water than in MW (Fig. 7c) is seen in the narrower buffer zone, where 17 Sv are transferred to class 4, the same rate of mass transfer as in the wide-zone case. Similarly, 10 Sv are transferred to class 5 within the class 4 buffer zone of

MN (Fig. 11b), as in class 4 of MW (Fig. 7d). In the Irminger Basin and Labrador Sea, however, the diapycnal transfers in MN (Fig. 11b) are significantly smaller than those in class 4 of MW (Fig. 7d), with a total of 4 Sv in MN, versus 8 Sv in MW, converted to the densest class from those two regions. Consequently, the transport around Cape Farewell is 13 Sv in class 5 of MN (not shown), versus 16 Sv in MW, and the southward deep transport across 48°N is 14 Sv, versus 18 Sv in MW.

In the high-resolution experiments HW and HN, the diapycnal transfers for classes 1 and 2 (not shown) differ from those in the MW and MN results in being moderately stronger (e.g., 17 Sv from class 1 to class 2 in both high-resolution experiments vs 14 Sv for the medium-resolution runs) and in displaying more detailed structure as a result of the finer grid resolution. In class 3, both HW (Fig. 12a) and HN (Fig. 13a) exhibit the high variability in diapycnal transfers noted in the medium-resolution results. Conversions to Class 4 within the buffer zone east of Greenland (concentrated closer to the northern wall in the narrow-zone HN) are 20 Sv in both HW and HN, exceeding the conversions that occurred in MW and MN by 3 Sv. Not surprisingly, the more inertial high-resolution cases exhibit a greater difference between the model-generated fields and those prescribed by Levitus (1982). Within class 4 of HW (Fig. 12b), 8 Sv are transferred to class 5 within the buffer zone, and an additional 14 Sv in the Irminger and Labrador Basins, which form a near-continuous region of sinking around the southern coast of Greenland. The total diapycnal transfer from class 4 to class 5 of HN (Fig. 13b) is at most 2 Sv less than that seen in HW. Within class 5, both high-resolution experiments carry 13 Sv around Cape Farewell and 22–23 Sv southward across 48°N, considerably larger southward deep transport values than those found in class 5 of the more viscous medium-resolution cases MW (18 Sv) and MN (14 Sv).

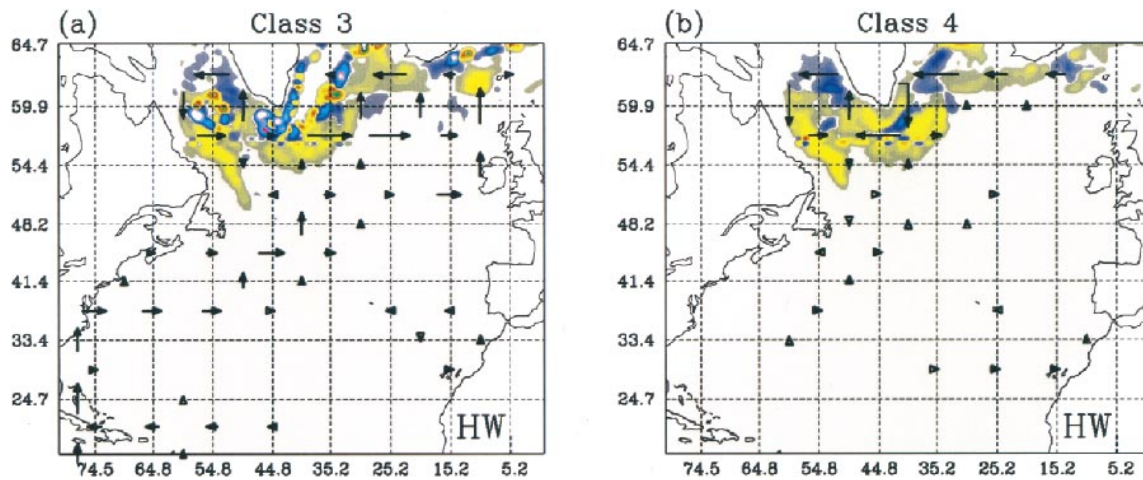


FIG. 12. As in Fig. 7 but for expt HW: (a) class 3, (b) class 4.

Although it was previously noted (section 4a; Figs. 1, 2) that the narrow buffer zones of experiment HN are less effective than those of HW in renewing the densest water mass in the model domain, the analysis of mass transport budgets by multilayer density classes does not reveal the gains or losses in mass incurred by individual layers. Comparison of the meridional overturning streamfunctions for HW (Fig. 4c) and HN (Fig. 4d), however, shows that the class 5 (layers 14–16) circulation in HN is concentrated toward the lighter density levels, as opposed to the more evenly distributed circulation of HW in the class 5 density range.

3) MODIFIED BUFFER ZONE—EXPERIMENT MWM

This experiment duplicates the base experiment MW in horizontal resolution (0.9°) and buffer zone width ($\sim 4^\circ$), while modifying the density structure in the Denmark Strait region of the northern buffer zone. Following Döscher et al. (1994), we replace the climatological data of Levitus (1982) in the boundary region, from $\sim 30^\circ$ – 40° W and at depths below 1000 m, with temperature and salinity values interpolated from the TTO section data given by Smethie and Swift (1989). Döscher et al. found that the use of this hydrographic data, which preserves the sharp density gradient appropriate to the Denmark Strait overflow water (DSOW; $\sigma_\theta \approx 27.95$), increased both the overturning strength and the associated northward heat transport in GFDL/CME experiments of varying horizontal resolution, relative to values obtained with relaxation to climatology. Since layer 16 ($\sigma_\theta = 27.92$) is the densest layer in our domain, we do not explicitly include in MWM the DSOW present in the Smethie and Swift (1989) hydrographic section. Rather, the modification of the initial conditions for MWM replicates the sharper tilt of the isopycnals present in the Denmark Strait hydrography (Fig. 1 of Döscher et al. 1994) and adds only a small amount of mass to layer 16 of MWM relative to that present in

the initial density structure of MW for that region, as determined by the Levitus (1982) climatology.

The mass budget analysis for the MWM results, averaged over the same 5-yr period as the base experiment, reveals essentially no difference from the MW analysis in the upper two density classes (not shown). In class 3, 18 Sv are converted to class 4 in the MWM buffer zone east of Greenland (Fig. 14a) (vs 17 Sv in MW; Fig. 7c) and are distributed within class 4 (Fig. 14b) in a similar configuration to that found in the same class of MW (Fig. 7d). In the modified experiment, 11 Sv reach class 5 from the class 4 buffer zone (vs 10 Sv in MW) and the conversions to class 5 in the Irminger Basin and in the Labrador Sea differ by only small, offsetting amounts in the two experiments. The southward flux of dense water across 48° N in class 5 of MWM (not shown) thus shows an increase of only 1 Sv relative to that in MW (Fig. 9b), and the annual mean meridional overturning streamfunctions and heat transport curves for the two experiments are nearly identical (Figs. 4, 5, for MW). Analysis of layer-by-layer box diagrams (not shown) for both MW and MWM indicates that the additional 1 Sv southward flux in class 5 of MWM lies within layer 16.

In contrast to these results for experiments MW and MWM, the Döscher et al. (1994) experiment with relaxation to unsmoothed hydrographic data in the Denmark Strait showed a 4 Sv increase in meridional overturning strength compared to the value obtained in the original GFDL/CME simulation with relaxation to climatology. In the Döscher et al. experiment, addition of the densest water present in the Smethie and Swift (1989) Denmark Strait hydrography ($\sigma_\theta \approx 27.95$), as well as inclusion of the sharper horizontal density gradient determined from that data (implying stronger geostrophic velocities through the section), allows passage of the DSOW signal across the GIS ridge despite the effects of cross-isopycnal mixing [diagnosed by Roberts et al. (1996)] and results in an increase in the strength

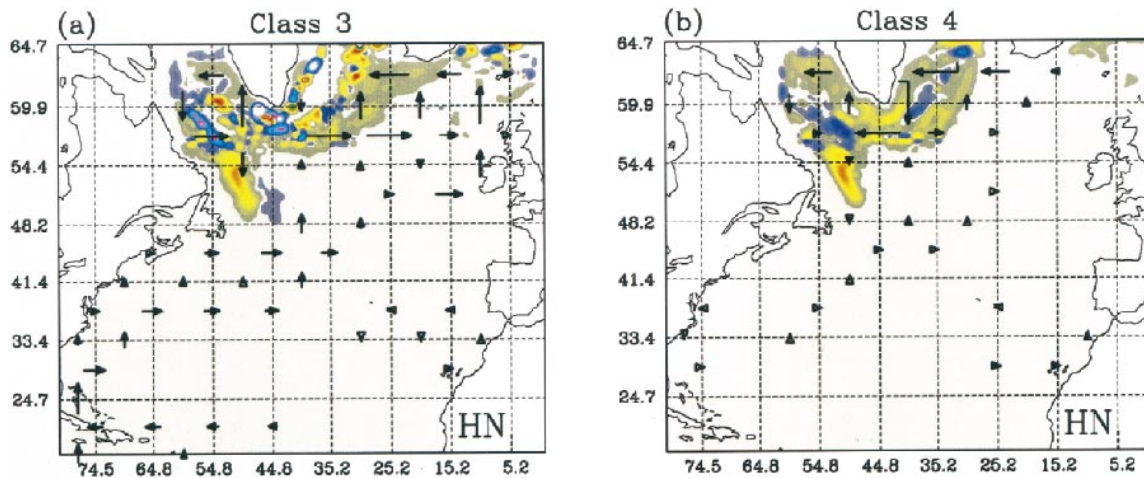


FIG. 13. As in Fig. 7 but for expt HN: (a) class 3, (b) class 4.

of the meridional overturning compared to that of their experiment forced by climatology. For the depth-coordinate model, it is essential to retain in the relaxation data the strong variations in density that signify the DSO. The smoothed nature of the Levitus (1982) climatology together with the coarse deep-water vertical resolution of the depth-coordinate model fail to provide realistic thermohaline forcing in the density range of lower NADW, so that the transport of that water mass is significantly underrepresented in the original GFDL/CME experiments upon which the Döscher et al. study was based. In our experiments, the dense water in either case—MW or MWM—is not subject to the numerically induced cross-isopycnal mixing that can occur in a depth-coordinate model, modifying the outflow properties as water crosses the ridge topography. The lower deep water represented in these density-coordinate simulations, whether produced within the buffer zones or convectively formed, retains its density characteristics

as it is transported to the south within class 5 (Figs. 7e, 9b).

Döscher et al. (1994) also found that the temperature range of the single-core deep southward flow in the initial GFDL/CME experiments was that of upper NADW (LSW) rather than of lower NADW. Their experiment replacing the Levitus (1982) climatology with hydrographic data from the Denmark Strait produced a meridional overturning cell with southward flow along the ocean bottom, at temperatures appropriate to the lower NADW, but without a separate path representing the LSW (see Fig. 9c of CSBB). Our medium-resolution wide-zone density-coordinate experiments MW and MWM also produce only a single path of deep southward flow (see Fig. 10a of CSBB), independent of the incorporation of smoothed climatology or raw hydrographic data in the northern restoring zone. Within that path the representation of NADW and of convectively formed water from the Labrador Sea are included, both

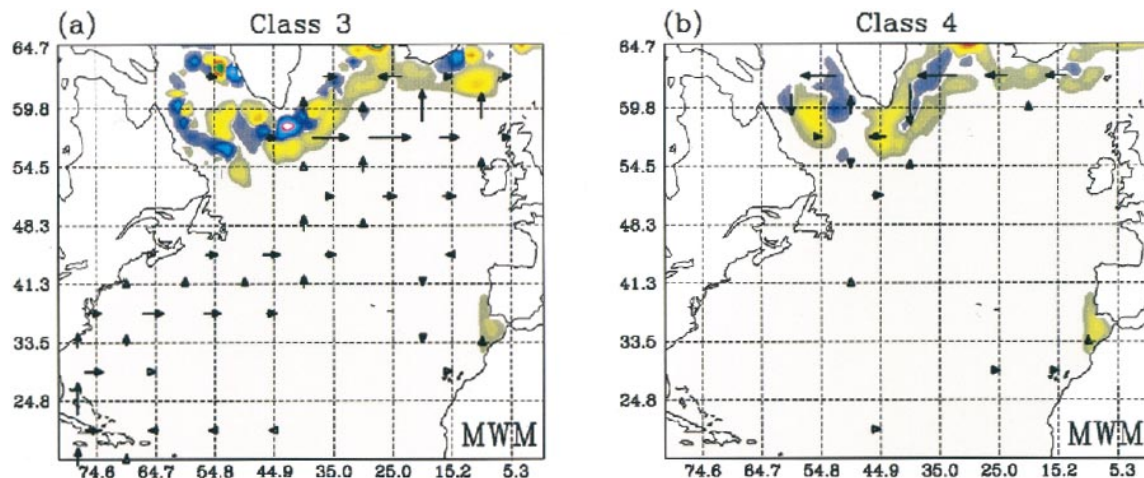


FIG. 14. As in Fig. 7 but for expt MWM: (a) class 3, (b) class 4.

flowing to the south at the density level of the densest model class.

4) COMPARISON WITH GFDL/CME EXPERIMENTS

Although we have gauged the model results by comparison to observational estimates, the design of our experiments has largely been intended to allow comparison to the results of similarly configured North Atlantic simulations, particularly the GFDL/CME depth-coordinate experiments studied by BBHD. We have not, however, attempted to determine if mechanisms related to differences in the two coordinate systems can affect the results of simulations incorporating buffer-zone relaxation. That topic has recently been addressed by Killworth (1999), with the conclusion that relaxation of temperature and salinity in depth-coordinate models can be considered equivalent to relaxation of either of those tracers, or of layer thickness, in density-coordinate models wherever the observed and model vertical density gradients are sufficiently close to one another. No conclusion is reached as to which type of model relaxation is "better," and Killworth (1999) points out that other model aspects influencing the results (especially at high resolution) are likely to dominate aspects related to relaxation.

BBHD have analyzed the results of GFDL/CME experiment N1-26.0, analogous to experiment MW in terms of horizontal resolution, buffer zone width, and mixing parameterization, and report ~ 17 Sv sinking across 1000 m, north of 47°N . The northern buffer zone contributes 13 Sv to this total in experiment N1-26.0, comparable to the 10 Sv of deep water that reaches class 5 from the similar-width relaxation region of MW. In the high-resolution GFDL/CME case N13-1, however, BBHD find that the narrow ($\frac{1}{3}^\circ$) northern buffer zone contributes only 4 Sv to the 13 Sv southward transport of NADW. In contrast, our analogous experiment HN includes 8 Sv reaching class 5 from the narrow relaxation region east of Greenland, only 2 Sv less than in MW.

In both MW and HN, the contribution to the simulated deep water formation from the Labrador Sea and from the Irminger Basin is greater than that found in either of the comparable GFDL/CME experiments. The model Labrador Basin contributes only 1 Sv to the overall deep water production in both experiments N1-26.0 and N13-1, versus deep water contributions from that region of 3 Sv in MW and 9 Sv in HN. BBHD state that although dense water is formed in the Labrador region of the GFDL/CME model basin at an annual rate comparable to that observed, a lack of horizontal processes to effectively drain the water from the model Labrador Sea may be the cause of the small contribution from this water mass to the model deep southward flow. Döscher and Redler (1997) confirm this supposition for the 1° GFDL/CME model, finding that enhanced convection in the Labrador gyre, and more effective drain-

age, can be achieved by decreasing the apparent temperature to which the surface values in that region are relaxed. In our density-coordinate simulations, the water converted from class 4 to class 5 in the Labrador Sea (e.g., Fig. 7d) is transported to the south along streamlines of deep flow such as those shown for MW in Fig. 9b, retaining its dense attributes by virtue of being confined to the three deepest isopycnal layers. Comparison of Figs. 9b and 10a of CSBB, showing the meridional overturning streamfunctions in depth coordinates for experiments N1-26.0 and MW, respectively, also illustrates the near-bottom southward transport of dense water in the latter experiment, carried out with MICOM, in contrast to the shallower overturning cell of the GFDL/CME results.

Although observational summaries (e.g., Schmitz 1996) do not describe a distinct Irminger Basin region of dense water production, all GFDL/CME experiments analyzed by BBHD indicate formation of deep water across 1000-m depth in the Irminger and Iceland Basins, at annual mean rates ranging from ~ 1 to 7 Sv. BBHD note that quasi-horizontal currents inclined against isobaths, such as those of the Reykjanes Ridge on the eastern side of the Irminger Basin, may result in downward-directed motion with the integral effect of sinking. However, BBHD do not find extremes of density or mixed layer depth in the Irminger or Iceland Basins, but only in the Labrador Sea, where evidence of deep winter convection is seen in the GFDL/CME simulations. Our experiments show evidence of deep winter mixing and formation of dense water in the Irminger Basin and in the Labrador Sea (e.g., Figs. 7d, 10a, for MW), both of which display maximum winter mixed layer densities that lie in the lower deep water range of class 5 (Fig. 10c).

Roberts et al. (1996) find dense water formation in the Irminger Basin in both their density-coordinate (MICOM) and depth-coordinate (GFDL) model experiments. In their GFDL results, mixed layer depths in the Irminger region remain relatively shallow (~ 500 m) even in the instance of dense water formation, consistent with the findings of BBHD for the GFDL/CME experiments. Roberts et al. attribute this shallow mixed layer to the existence of a homogeneous subsurface water mass that originates from the mixed overflow water and stabilizes the water column downstream of the GIS ridge. In the Roberts et al. MICOM experiments, however, both the maximum mixed layer depth and subpolar gyre surface density are found in the Irminger Basin, as a result of deep winter mixing, rather than in the Labrador Sea as observations indicate (McCartney and Talley 1982). Roberts et al. speculate that the predominance of the Irminger region over the Labrador in regard to dense water formation in their density-coordinate results may be related to a relatively weak simulated East Greenland Current (EGC). In reality, that current supplies cold, fresh water to the Irminger surface layer, stratifying the water column and thus inhibiting

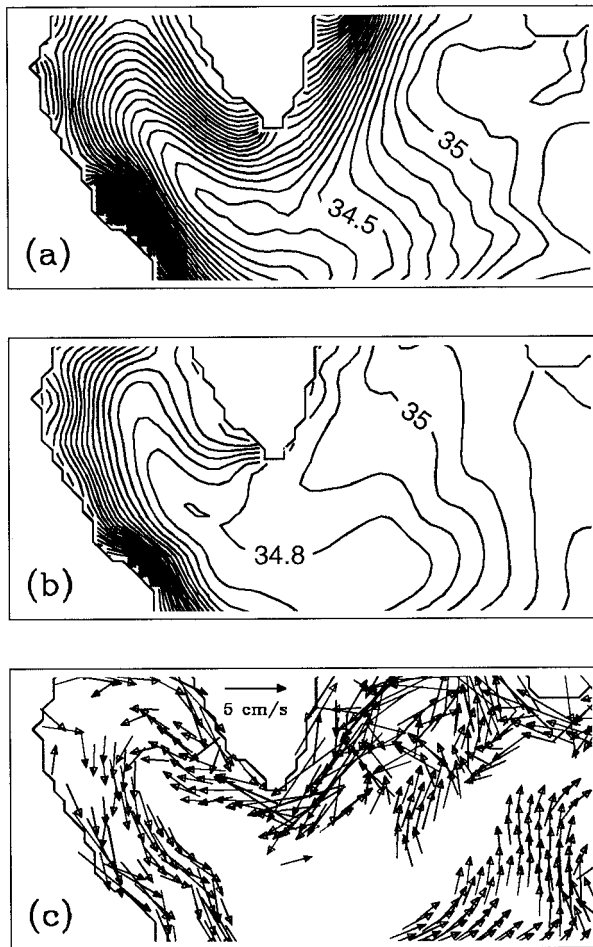


FIG. 15. (a) Winter surface salinity near Greenland, Levitus (1982) climatology. (b) Surface salinity near Greenland, expt MW, Mar, year 1. (c) Surface velocity near Greenland, expt MW, Mar, year 1. Contour interval for salinity 0.1 psu.

convective overturning such as that which deepens the Labrador Sea mixed layer in winter (McCartney and Talley 1982).

The winter salinity gradient indicative of the fresh polar-origin surface water that leads into the EGC, stabilizing the Irminger Basin water column, can be seen along the eastern Greenland coast in the Levitus (1982) climatology, close to the northern wall of our model domain (Fig. 15a). Despite surface salinity relaxation to the Levitus values in our experiments [weakened by the proportionality of the relaxation time to the depth of the mixed layer (CSBB)], the gradient appears to be substantially attenuated within a few months of model integration time (Fig. 15b). As westward flow along the artificial wall, leading into southward flow along Greenland, carries warm, relatively salty water to the model Irminger Basin (Fig. 15c), the water column in that region is destabilized, permitting the onset of deep mixing and the subsequent lower deep water mass formation that is seen in our results (e.g., Fig. 7d, for expt MW).

Because the deep winter mixing noted in the Irminger region of our experiments is limited both in space and in time (Fig. 10c), the diapycnal mass transfers occurring in that basin do not add any detectable amount of mass in the 5-yr mean to layer 16, the densest water mass of our domain. Box diagrams for individual layers of the 5-yr-mean experiment MW results (not shown) indicate, for example, that of the 5 Sv converted in the Irminger region from class 4 (Fig. 7d) to class 5 (layers 14, 15, 16), 2 Sv circulate around Cape Farewell within layer 14, while 3 Sv reach layer 15 and join the flow to the south within that layer. In the narrow-zone experiment MN, the 2 Sv mass transfer from the Irminger region of class 4 into class 5 (Fig. 11b) is received only by layer 14. These transfers into class 5 are detectable in the year 25 overturning streamfunctions for the two experiments, from layer 13 to layer 14 in MN (Fig. 4b), and from layer 13 to layer 14 to layer 15 in MW (Fig. 4a), near 60°N. The wider relaxation region in MW provides stronger water mass conversions east of Greenland than those that occur in MN and, in addition, serves to protract the southward flow along the coast that carries warm, salty water to the Irminger Basin (Fig. 15c). Sinking in the Irminger region is thus more notable in the results of the wide-zone experiment MW than in those of the narrow-zone MN.

5. Summary and discussion

The design and implementation of the northern boundary conditions are crucial factors in the ability of a North Atlantic ocean model to properly simulate the water mass transformations that occur in high latitudes and the subsequent pathways into the interior basin. The choice made in the CME to employ buffer zones at a closed northern boundary—that is, an artificial wall—across the GIS ridge has raised questions in depth-coordinate model studies regarding the forcing used in the relaxation (Döscher et al. 1994), the choice of grid resolution (Beckmann et al. 1994), and the width of the buffer zone itself (BBHD). In addition, the study carried out by CSBB examined the effect of model design (in particular the choice of vertical coordinate) on the ability of buffer zone-based simulations to properly represent the North Atlantic meridional overturning circulation and the associated northward transport of heat.

In the present work, we have examined the results of several North Atlantic model experiments carried out with the density-coordinate MICOM, varying both the horizontal grid resolution (0.9° and $\frac{1}{3}^\circ$) and the width of the northern buffer zone (4° and $\frac{1}{3}^\circ$). We have sought to determine whether or not the solutions of our four principal experiments depend on the factors of either medium or high resolution, or of either wide or narrow buffer zones. With an additional experiment to address the issue of modification of the buffer zone forcing, we have replicated the major points of the depth-coordinate

model studies of BBHD, Beckmann et al. (1994), and Döscher et al. (1994).

Analysis of the results of experiments MW, MN, HW, and HN focused first on quantities evolving in time, namely, the basin-averaged layer volumes, the changes in mass for a deep-water layer, and the spreading within that layer of water injected with a passive tracer. The apparent similarity in basin-averaged layer volume evolution for several of the model cases was found to conceal differences in the geographical distribution of changes in layer thickness over time among the experiments. Stronger conversions to dense water in the sub-polar gyre region of the deep water layer were seen in the high-resolution, wide-zone case HW than in the medium-resolution MW, while both of the narrow-zone experiments MN and HN showed signs of a less effective renewal over time of the densest water mass in the domain. Similarly, evidence of the relatively constricted spread of tracer-injected water (indicative of water mass modification in the model buffer zones) was seen in the tracer diagrams for the narrow-zone cases MN and HN, although in each of those experiments the model DWBC reached nearly as far south as in the corresponding wide-zone experiments MW and HW. Both of the high-resolution (and less viscous) simulations, however, exhibited deep boundary currents that extended farther to the south along the western boundary than those of their medium-resolution counterparts.

The time-averaged quantities of meridional overturning streamfunction and northward heat transport provided more concrete evidence that high grid resolution coupled with a wide northern buffer zone produces, for our experiments, the strongest circulation in the vertical-meridional plane. Both of the wide-zone cases MW and HW give higher maximum overturning rates than their narrow-zone counterparts, but an even larger difference in the maximum overturning was seen for the high-resolution cases as compared to those with medium-resolution grids. The annual mean northward heat transport showed differences among the maximum values for the four experiments corresponding in relative order to those for the overturning strength, with the greater total transport for the more inertial high-resolution experiments being attributed to a correspondingly greater gyre component contribution in those simulations.

The 5-yr-average mass transport budgets also indicated stronger water mass modifications for the high-resolution experiments, leading to stronger deep flows down the western boundary in the densest model class than in the medium-resolution cases. However, in each experiment the southward transport across 48°N in the densest class is comparable to observational estimates. The model results in the Irminger and Labrador Basins, however, do not conform to such estimates in several respects. Our experiments do not reproduce the two paths, at distinct density levels, of upper NADW (LSW) and lower NADW within the DWBC, and the Irminger

Basin formation of a deep water mass in each of our model cases (attributable to a weakened surface salinity gradient in the Irminger region and to the presence of the artificial northern wall) has no reported real-world analog.

Comparison of the present results to those of the GFDL/CME experiments first showed that a reduction in buffer zone width in our simulations does not lead to a reduction in net overturning rates as found in the depth-coordinate results of BBHD. The maximum meridional overturning for the narrow-zone HN, 21 Sv, exceeds by 4 Sv the maximum found for the wide-zone case MW. The comparable experiments in BBHD show overturning rates of 13 Sv for the high-resolution narrow-zone experiment N13-1, 4 Sv less than for the medium-resolution wide-zone experiment N1-26.0. Similarly, the Beckmann et al. (1994) finding of a decrease in meridional overturning rates with increasing horizontal resolution (from $\frac{1}{3}^\circ$ to $\frac{1}{6}^\circ$ in their experiments, with buffer zone width held constant) does not hold for our model cases when comparing 0.9° and $\frac{1}{3}^\circ$ results. The modified simulation MWM followed the experiment of Döscher et al. (1994) in using relaxation based on a hydrographic section in a region of the northern buffer zone, but produced negligible differences from the MW solution (obtained with relaxation to climatology), as opposed to the increased overturning strength found in the depth-coordinate Döscher et al. results.

In a depth-coordinate model, strong numerical cross-isopycnal mixing over the North Atlantic ridge topography leads to a relatively shallow and light simulated NADW (Roberts et al. 1996), while the density-coordinate formulation, which incorporates diapycnal mixing only as explicitly prescribed, is capable of retaining the characteristics of its densest water masses throughout the integration (CSBB). The resulting deep-water densities, however, may exceed climatological values, as found in the DYNAMO (1997) isopycnal experiment. That simulation, extending to 70°N, seeks to explicitly model the dense overflows, but omits parameterization of the entrainment processes that occur outside the model northern relaxation zone. In the buffer zone approach adopted for the CME experiments, relaxation to climatology is intended to represent both the production of dense water outside the model domain as well as the subsequent entrainment of lighter water into the overflows, so that reasonable characteristics are obtained for the model-generated NADW. The DYNAMO (1997) group suggest that deep-water properties in a density-coordinate model may be made more realistic by increased diapycnal mixing, especially in areas of strong topographic slope, and by the inclusion of thermobaric effects in the equation of state. These topics are, respectively, the subject of recent studies by Hallberg (2000) and by Sun et al. (1999).

While the results of our experiments do not appear to depend inordinately on buffer zone width or horizontal resolution (although the high-resolution wide-

zone case HW may be said to give the “best” solution, in terms of the strength of water mass conversions occurring therein), they do indicate elements of model design that call for continued study. In experiments focusing on the Atlantic, the use of σ_2 (rather than σ_θ) as the model’s representation of density will enable simulation of the AABW that upwells in northern midlatitudes, while improvements in vertical (density) resolution and appropriate definition of the isopycnic layers are expected to allow the solutions to represent the upper NADW (LSW) path within the DWBC and, potentially, such distinct types as the southern Labrador Sea water identified by Pickart (1992). Continued study of these vertical coordinate issues, together with increases in computing power that permit greater horizontal and vertical resolution, will lead to more accurate representations of the three-dimensional structure of the North Atlantic circulation.

Acknowledgments. We thank Claes G. H. Rooth and Yanli Jia for valuable discussions. Support was provided by the National Science Foundation through Grants OCE-9206643 and OCE-9531852. Computations were carried out on the CRAY Y-MP8/864, CRAY J90se, and CRAY T3D at the National Center for Atmospheric Research (NCAR). NCAR is sponsored by the National Science Foundation.

APPENDIX

Mass Transport Budget Computations

To document the model water mass transformations, we calculate “box budgets” of mass transport for the results of the experiments listed in section 2. The model mixed layer and 15 isopycnic layers are divided into five density classes, based on Schmitz’s (1996) division of the global ocean (Table 3), with mixed layer water in each grid column included in the class to which its density belongs.

The model region is divided into nominally square boxes with sides of length $\sim 9^\circ$ longitude (see, e.g., Fig. 7). Intra-class mass transport fluxes are indicated by arrows that cross box boundaries, and are not shown if less than 1 Sv. To illustrate the diapycnal mass transfers that are the focus of this study, the budget-box display is overlaid in classes 1–4 by a color-contoured field representing the diapycnal fluxes as calculated on an individual-grid-box basis. The contours represent mass exchange between the class being viewed and the next-heavier class, with colors at the negative end of the scale indicating a conversion to denser water (i.e., a transfer into the next density class), and colors at the positive end of the scale indicating conversion to lighter water (i.e., a transfer into the present class from the next). In order to remove the dependence of the diapycnal flux magnitude on the model grid size, which varies with latitude, the fluxes are normalized by the ratio of the

area of the large (9°) budget box to which they belong to the area of the individual grid box. The color field is thus contoured in units of “Sverdrups per budget box,” independent of latitude.

For each grid box, the diapycnal flux is computed by continuity considerations, also taking into account any change in box volume for the class in question over the time period of the budget calculation. For the model experiments listed in section 2, that calculation is performed for a 5-yr period that begins and ends in September, the month in which the mixed layer is normally at its shallowest over the model basin. This choice minimizes the volume difference term that enters into the budget calculation by reducing the effect of layer thickness changes that occur during entrainment and detrainment processes at other times of the year, changes that may exhibit large interannual variations. The averaging period is sufficiently long to permit calculation of the standard deviation of the annual means from the 5-yr mean for both the intra-class and diapycnal fluxes, so that the internal model variability arising from nonlinear effects can be studied.

REFERENCES

- Beckmann, A., C. W. Böning, C. Köberle, and J. Willebrand, 1994: Effects of increased horizontal resolution in a simulation of the North Atlantic Ocean. *J. Phys. Oceanogr.*, **24**, 326–344.
- Bleck, R., and E. P. Chassignet, 1994: Simulating the oceanic circulation with isopycnic-coordinate models. *The Oceans: Physical-Chemical Dynamics and Human Impact*, S. K. Majumdar, E. W. Miller, G. S. Forbes, R. F. Schmalz, and A. A. Panah, Eds., The Pennsylvania Academy of Science, 17–39.
- Böning, C. W., and P. Herrmann, 1994: Annual poleward heat transport in the ocean. Results from high-resolution modeling of the North and Equatorial Atlantic. *J. Phys. Oceanogr.*, **24**, 91–105.
- , W. R. Holland, F. O. Bryan, G. Danabasoglu, and J. C. McWilliams, 1995: An overlooked problem in model simulations of the thermohaline circulation and heat transport in the Atlantic Ocean. *J. Climate*, **8**, 515–523.
- , F. O. Bryan, W. R. Holland, and R. Döscher, 1996: Deep-water formation and meridional overturning in a high-resolution model of the North Atlantic. *J. Phys. Oceanogr.*, **26**, 1142–1164.
- Bryan, F. O., and W. R. Holland, 1989: A high resolution simulation of the wind- and thermohaline-driven circulation in the North Atlantic Ocean. *Parameterization of Small-Scale Processes. Proc. Aha Huliko’a Hawaiian Winter Workshop*, University of Hawaii, P. Müller and D. Anderson, Eds. 17 pp.
- Bryan, K., 1969: A numerical model for the study of the world ocean. *J. Comput. Phys.*, **4**, 347–376.
- , 1982: Poleward heat transport by the ocean: Observations and models. *Annu. Rev. Earth Planet. Sci.*, **10**, 15–38.
- Chassignet, E. P., L. T. Smith, R. Bleck, and F. O. Bryan, 1996: A model comparison: Numerical simulations of the North and equatorial Atlantic oceanic circulation in depth and isopycnic coordinates. *J. Phys. Oceanogr.*, **26**, 1849–1867.
- Clarke, R. A., 1984: Transport through the Cape Farewell–Flemish Cap section. *Rapp. P.-V. Réun. Cons. Int. Explor. Mer*, **185**, 120–130.
- , and J.-C. Gascard, 1983: The formation of Labrador Sea Water. Part I: Large-scale processes. *J. Phys. Oceanogr.*, **13**, 1764–1778.
- Cox, M. D., 1984: A primitive equation three-dimensional model of the ocean. Tech. Rep. 1, GFDL/NOAA, Princeton University,

- NJ, 144 pp. [Available from GFDL, P.O. Box 308, Princeton, NJ 08542.]
- Döscher, R., and R. Redler, 1997: The relative importance of northern overflow and subpolar deep convection for the North Atlantic thermohaline circulation. *J. Phys. Oceanogr.*, **27**, 1894–1902.
- , C. W. Böning, and P. Herrmann, 1994: Response of circulation and heat transport in the North Atlantic to changes in thermohaline forcing in northern latitudes. A model study. *J. Phys. Oceanogr.*, **24**, 2306–2320.
- DYNAMO Group, 1997: DYNAMO: Dynamics of North Atlantic Models. Simulation and assimilation with high resolution models. Institut für Meereskunde an der Universität Kiel, 334 pp.
- Fine, R. A., and R. L. Molinari, 1988: A continuous deep western boundary current between Abaco (26.5°N) and Barbados (13°N). *Deep-Sea Res.*, **35**, 1441–1450.
- Gerdes, R., and C. Köberle, 1995: On the influence of DSOW in a numerical model of the North Atlantic general circulation. *J. Phys. Oceanogr.*, **25**, 2624–2642.
- Hall, M. M., and H. L. Bryden, 1982: Direct estimates and mechanisms of ocean heat transport. *Deep-Sea Res.*, **29**, 339–359.
- Hallberg, R., 2000: Time integration of diapycnal diffusion and Richardson number dependent mixing in isopycnal coordinate ocean models. *Mon. Wea. Rev.*, in press.
- Han, Y.-J., 1984: A numerical World Ocean general circulation model. Part II: A baroclinic experiment. *Dyn. Atmos. Oceans*, **8**, 141–172.
- Hellerman, S., and M. Rosenstein, 1983: Normal monthly wind stress over the world ocean with error estimates. *J. Phys. Oceanogr.*, **13**, 1093–1104.
- Holland, W. R., and F. O. Bryan, 1994: Sensitivity studies on the role of the ocean in climate change. *Ocean Processes in Climate Dynamics: Global and Mediterranean Examples*, P. Malanotte-Rizzoli and A. R. Robinson, Eds., 111–134.
- Hsuing, J., R. E. Newell, and T. Houghtby, 1989: The annual cycle of oceanic heat storage and ocean meridional heat transport. *Quart. J. Roy. Meteor. Soc.*, **115**, 1–28.
- Killworth, P. D., 1999: Relaxation toward observations in level and isopycnal models. *J. Atmos. Oceanic Technol.*, **16**, 983–986.
- Klinck, J. M., 1995: Thermohaline structure of an eddy-resolving North Atlantic model. The influence of boundary conditions. *J. Phys. Oceanogr.*, **25**, 1174–1195.
- Levitus, S., 1982: *Climatological Atlas of the World Ocean*. NOAA Prof. Paper No. 13, U.S. Govt. Printing Office, 173 pp.
- Macdonald, A. M., and C. Wunsch, 1996: An estimate of global ocean circulation and heat fluxes. *Nature*, **382**, 436–439.
- Mauritzen, C., and S. Häkkinen, 1999: On the relationship between dense water formation and the meridional overturning cell. *Deep-Sea Res.*, **46**, 877–894.
- McCartney, M. S., 1993: Crossing of the equator by the Deep Western Boundary Current in the western Atlantic Ocean. *J. Phys. Oceanogr.*, **23**, 1953–1974.
- , and L. D. Talley, 1982: The subpolar mode water of the North Atlantic. *J. Phys. Oceanogr.*, **12**, 1169–1188.
- Molinari, R. L., E. Johns, and J. Festa, 1990: The annual cycle of meridional heat flux in the Atlantic Ocean at 26.5°N. *J. Phys. Oceanogr.*, **20**, 476–482.
- Pickart, R. S., 1992: Water mass components of the North Atlantic deep western boundary current. *Deep-Sea Res.*, **39**, 1553–1572.
- Redler, R., and C. W. Böning, 1997: Effect of the overflows on the circulation in the subpolar North Atlantic: A regional model study. *J. Geophys. Res.*, **102**, 18 529–18 552.
- Roberts, M. J., R. Marsh, A. L. New, and R. A. Wood, 1996: An intercomparison of a Bryan–Cox type ocean model and an isopycnal ocean model. Part I: The subpolar gyre and high-latitude processes. *J. Phys. Oceanogr.*, **26**, 1495–1527.
- Schmitz, W. J., Jr., 1995: On the interbasin-scale thermohaline circulation. *Rev. Geophys.*, **33**, 151–173.
- , 1996: On the world ocean circulation. Vol. 1, Woods Hole Oceanographic Institution Tech. Rep. WHOI-96-03, 141 pp. [Available from Woods Hole Oceanographic Institution, Woods Hole, MA 02543.]
- , and M. S. McCartney, 1993: On the North Atlantic circulation. *Rev. Geophys.*, **31**, 29–49.
- Smethie, W. M., Jr., and J. H. Swift, 1989: The tritium:krypton-85 age of Denmark Strait overflow water and Gibbs Fracture Zone water just south of Denmark Strait. *J. Geophys. Res.*, **94**, 8265–8275.
- , R. A. Fine, A. Putzka, and E. P. Jones, 1999: Tracing the flow of North Atlantic Deep Water using chlorofluorocarbons. *J. Geophys. Res.*, in press.
- Sun, S., 1997: Compressibility effects in the Miami Isopycnal Coordinate Ocean Model. Ph.D. dissertation, University of Miami, 138 pp. [Available online at http://panoramix.rsmas.miami.edu/micom/micom_refs.html.]
- , R. Bleck, C. G. H. Rooth, J. Dukowicz, E. P. Chassignet, and P. Killworth, 1999: Inclusion of thermobaricity in isopycnal-coordinate ocean models. *J. Phys. Oceanogr.*, **29**, 2719–2729.
- Talley, L. D., and M. S. McCartney, 1982: Distribution and circulation of Labrador Sea Water. *J. Phys. Oceanogr.*, **12**, 1189–1205.
- Trenberth, K. E., and A. Solomon, 1994: The global heat balance: Heat transports in the atmosphere and ocean. *Climate Dyn.*, **10**, 107–134.
- U.S. WOCE Office, 1993: U.S. WOCE Implementation Plan. U.S. WOCE Office, College Station, TX, 146 pp. [Available from U.S. WOCE Office, Texas A&M University, College Station, TX 77843-3146.]